

Boom and Receptacle Autonomous Air Refueling Using Visual Snake Optical Sensor

James Doebbler, Theresa Spaeth,
and John Valasek
Texas A&M University, College Station, TX 77843-3141

Mark J. Monda and Hanspeter Schaub
Virginia Polytechnic Institute, Blacksburg, VA 24061-0203

Simulated Reprint from

Journal of Guidance, Navigation and Control

Volume 30, Number 6, Nov.–Dec., 2007, Pages 1753–1769



A publication of the
American Institute of Aeronautics and Astronautics, Inc.
1801 Alexander Bell Drive, Suite 500
Reston, VA 22091

Boom and Receptacle Autonomous Air Refueling Using Visual Snake Optical Sensor

James Doebbler,* Theresa Spaeth,†
and John Valasek‡

Texas A&M University, College Station, TX 77843-3141

Mark J. Monda§ and Hanspeter Schaub¶

Virginia Polytechnic Institute, Blacksburg, VA 24061-0203

Autonomous air refueling is an important capability for the future deployment of unmanned air vehicles, since it permits unmanned air vehicles to be ferried in flight to overseas theaters of operation instead of being shipped unassembled in containers. This paper demonstrates the feasibility of precise and reliable boom and receptacle autonomous air refueling, without a human operator or supervisor, for non micro sized unmanned air vehicles. The system is composed of a vision sensor based on active deformable contour algorithms (visual snakes) and its relative navigation system integrated with a boom controller. The sensor camera is mounted on the tanker aircraft near the boom, and images a single passive target image painted near the refueling receptacle on a receiver unmanned air vehicle. Controllers are developed in the paper for the refueling boom, and the station keeping controllers of the receiver unmanned air vehicle and tanker aircraft. Performance and feasibility of the total system is demonstrated by simulated docking maneuvers in the presence of various levels of turbulence. Results presented in the paper show that the integrated sensor and controller enables precise boom and receptacle air refueling, including consideration of realistic measurement errors and disturbances.

I. Introduction

Unmanned Air Vehicles (UAVs) are playing an important role in today's military initiatives. They are invaluable in locating time critical targets, reporting enemy positions and movements to battlefield commanders, and destroying strategic targets or lethal ground systems. Additionally, these unmanned systems are being designed to remain in flight for time periods of 18 hours or more. Unfortunately, these vehicles will have to return to their base of operations to obtain additional fuel. This limitation creates a deployment and logistics challenge for battlefield commanders.¹

There are currently two approaches used for air refueling. The probe-and-drogue refueling system is the standard for the United States Navy and the air forces of most other nations. In this method, the tanker trails a hose with a flexible "basket", called a drogue, at the end. The drogue is aerodynamically stabilized. It is the responsibility of the pilot of the receiver aircraft to maneuver the receiver's probe into the drogue. This method is used for small, agile aircraft such as fighters because both the hose and drogue are flexible and essentially passive during re-fueling. It also does not require a human operator on the tanker dedicated solely to performing the refueling operation.^{2,3,4} Autonomous in-flight refueling using a probe-and-drogue system is basically a docking situation that requires centimeter level accuracy in the relative position of the refueling probe (from the receiving aircraft) with respect to the drogue (from the tanker) during the end-game. This specification is based on the geometry of the existing probe and drogue hardware, and the need to ensure that the tip of the probe contacts only the inner sleeve of the receptacle and not the more lightly constructed and easily damaged shroud.¹ Examples of probe and drogue controllers in the recent literature include a reference observer tracking controller,^{5,6} and a linear controller using methods from differen-

tial game theory.⁷

The United States Air Force uses the flying boom developed by Boeing. The boom approach is supervised and controlled by a human operator from a station near the rear of the tanker aircraft. This person is responsible for "flying" the boom into the refueling port on the receiver aircraft. In this method, the role of the receiver aircraft is to maintain a proper refueling position with respect to the tanker, and leave the precision control function to the human boom operator in the tanker.³

Several models of receiver aircraft are currently under development for boom and receptacle air refueling. To protect proprietary data associated with competing designs, Reference 8 develops an equivalent model that is representative in performance and maneuvering characteristics of a tailless UAV. The intent is to create a robust refueling design applicable to a range of future unmanned vehicles. This model is developed from a specification created by a panel of experts at the Air Force Research Laboratory, with inputs from contractors. Additional receiver aircraft models and simulations have been developed using the Panavia Tornado combat aircraft making contact with the VC10 tanker aircraft;⁹ for a tailless receiver aircraft with innovative control effectors and thrust vectoring capability that includes the effect of time-varying mass and inertia properties associated with the fuel transfer, the tanker's vortex induced wind effect, and atmospheric turbulence;¹⁰ and simulation environment modeling the tanker aircraft plus the receiver UAV plus a flexible refueling boom modeled with finite elements.¹¹ Reference 12 has taken the further step of comparing wind tunnel results of a delta wing UAV flying behind a KC-135R with analytical predictions from a planar vortex lattice code. Both the predictions and data show wake interference effects on the UAV that vary significantly with relative lateral and vertical position, and weakly with relative longitudinal position. The distribution of lift between the tanker wing and tail was shown to have a strong effect on the receiver aerodynamics. Finally, simulation models and environments have also been created for human operator-in-the-loop boom and receptacle refueling. These permit the evaluation of a prototype control station interface for controlling multiple UAVs.^{13,14}

While a Linear Quadratic Regulator (LQR) controller¹⁵ and a Proportional Navigation and Guidance (PNG) controller¹⁶ have been designed for boom and receptacle autonomous air refueling

*Graduate Research Assistant, Flight Simulation Laboratory, Aerospace Engineering Department. Student Member AIAA. james.doebbler@tamu.edu

†Graduate Research Assistant, Flight Simulation Laboratory, Aerospace Engineering Department. Member AIAA. thspaeth@tamu.edu

‡Associate Professor and Director, Flight Simulation Laboratory, Aerospace Engineering Department. Associate Fellow AIAA. valasek@tamu.edu

§Graduate Research Assistant, Aerospace and Ocean Engineering Department. Student Member AIAA. mjmonda@vt.edu

¶Assistant Professor, Aerospace and Ocean Engineering Department. Associate Fellow AIAA. schaub@vt.edu

¹Personal conversation with M. Bandak, Sargent Fletcher Inc., January 2002

assuming the use of generic relative position sensor, practical maturation of the capability requires several issues to be addressed, the most fundamental being the availability of sufficiently accurate/reliable relative motion sensors.¹⁷ Some methods that have been considered for determining relative position in a refueling scenario include measurements derived from the Global Positioning System (GPS), measurements derived from both passive and active machine vision, and visual servoing with pattern recognition software.^{18, 19, 20, 21, 22} GPS measurements have been made with 1 cm to 2 cm accuracy for formation flying, but problems associated with lock-on, integer ambiguity, low bandwidth, and distortions due to wake effects from the tanker present challenges for application to in-flight refueling. Pattern recognition codes are not sufficiently reliable in all lighting conditions, and with adequate fault tolerance, may require large amounts of computational power in order to converge with sufficient confidence to a solution.^{18, 19, 20}

Machine vision based techniques use optical markers to determine relative orientation and position of the tanker and the UAV. References^{11, 23} use a fuzzy sensor fusion strategy, featuring a combination of GPS-based and artificial vision-based measurements. The drawback of the machine vision based techniques is the assumption that all the optical markers are always visible and functional. Reference 24 proposes an alternative approach where the position estimation does not depend on optical markers but on feature extraction methods using specific corner detection algorithms. Special emphasis was placed on evaluating the accuracy, required computational effort, and robustness to different sources of noise. Closed loop simulations were performed using a detailed Simulink-based simulation environment to reproduce boom and receptacle docking maneuvers.

Another approach is an active vision based navigation system called VisNav. VisNav provides high precision six degree-of-freedom information for a real-time navigation application.^{25, 26, 27} VisNav is a cooperative vision technology in which a set of beacons mounted on a target body (e.g., the receiver aircraft) are supervised by a VisNav sensor mounted on a second body (e.g., the boom). VisNav structures the light in the frequency domain, analogous to radar, so that discrimination and target identification are near-trivial even in a noisy optical ambient environment. Controllers that use the VisNav sensor have been developed and evaluated specifically for probe and drogue autonomous air refueling.^{5, 6, 28, 29, 30} In principle, the VisNav system could work with legacy boom and receptacle refueling systems since the only major equipment changes are mounting the VisNav sensor to the boom and attaching four or more Light Emitting Diode (LED) beacon lights to the forebody of the receiver aircraft, or vice versa.

Another class of visual sensing methods are the active deformable contour algorithms. These methods segment the target area of the image by having a closed, non-intersecting contour iterate across the image and track a target. In 1987 Kass et al. proposed the original active deformable model to track targets within an images stream.³¹ They are also known as visual snakes. For application to the end game docking problem of autonomous air refueling, a visual snake optical sensor mounted on the boom would acquire and track a color target painted on the receiver aircraft, and develop a relative navigation solution which is then passed to a boom control system. This approach does not use pattern recognition, is passive, and highly robust in various lighting conditions.³² Although it does not provide six degree-of-freedom data, this is not a penalty for boom and receptacle autonomous refueling because the boom requires only two rotations and one translation to successfully engage the receptacle.

Referring to Fig. 1, the system proposed in this paper is comprised of a receiver aircraft (in this case a UAV) equipped with a GPS sensor, and an onboard flight controller which permits it to station keep in a 3D box of specified dimensions, relative to the tanker aircraft. The receiver aircraft has a visual docking target painted on its forebody, similar to the target painted on the forebody of the B-1B in Fig. 2. The tanker aircraft is equipped with two sensors dedicated to autonomous air refueling. The first sensor accurately measures the angular position of the boom at the pivot point, as well as the length of the boom, thereby providing a mea-

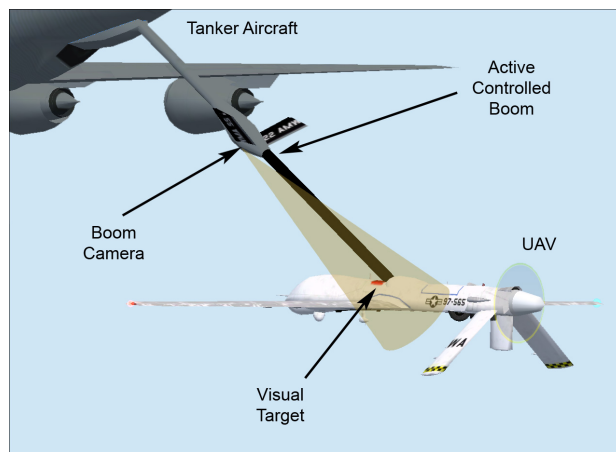


Figure 1: Conceptual Image of a KC-135 Refueling a Predator UAV



Figure 2: B-1B Lancer Refueling From a KC-135 Using Boom and Receptacle Method

surement of the tip of the boom. The second sensor is the visual snake sensor, which is mounted on the rear of the tanker and oriented so that it possesses a clear, unobstructed field-of-view of the visual docking target painted on the receiver aircraft's forebody. For night refueling operations, the visual target painted on the receiver aircraft is illuminated by a light installed on the tanker. An automatic control system for the refueling boom receives estimates of the refueling receptacle position from the visual snakes sensor, and steers the boom tip into it. There are no controller commands which would require a high speed, high bandwidth data link being passed between the tanker and receiver aircraft. A communication link handles initiation and termination of the refueling sequence. Fig. 3 shows the data flow for the proposed autonomous air refueling system.

This paper develops a vision based relative navigation system that uses a visual snakes optical sensor integrated with an automatic boom controller for autonomous boom and receptacle air refueling, without a human operator or supervisor. The capability of this system to accurately estimate the position of the receptacle, and then automatically steer the boom into it in light and moderate atmospheric turbulence conditions, is demonstrated using non real-time simulation. Detailed software models of the optical sensor system are integrated with the boom and station keeping controllers, and evaluated with refueling maneuvers on a six degree-of-freedom simulation. Docking maneuver test cases from initial positioning offsets in still air and in turbulence, are used to evaluate the

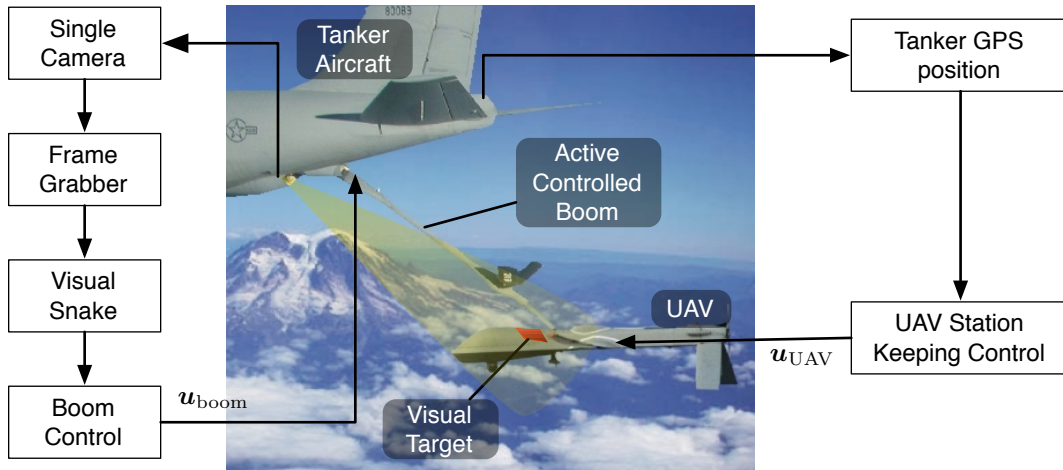


Figure 3: Data Flow for the Proposed Air Refueling System using the Visual Snake Sensor

combined performance of the optical sensor, boom controller, and station keeping controller system. For the refueling scenario investigated here, only the end-game docking maneuver is considered. It is assumed that the tanker and receiver have already rendezvoused, and that the tanker is flying straight ahead at constant speed and altitude. The receiver aircraft is positioned aft of the tanker in trimmed flight, and an onboard flight controller maintains position within a 3D box relative to the tanker.

The paper is organized as follows. First the basic working principles and components of the visual snakes navigation sensor are presented in Section II., detailing the algorithm and navigation solution, performance, target setup using perspective projection, and error sensitivities. A description of the reference frames and vector definitions used in the development of the dynamical models is presented in Section III.. The linear state-space models for the refueling boom and aircraft are developed in Sections IV. and V., respectively. Section VI. details the derivation of the Proportional-Integral-Filter optimal Nonzero Setpoint with Control Rate Weighting (PIF-NZSP-CRW) boom docking control law. The station keeping controller used for both the receiver and tanker aircraft is developed in Section VII.. In Section VIII., test cases using the Dryden gust model with light and moderate turbulence are presented to assess system performance and disturbance accommodation characteristics in the presence of exogenous inputs. Finally, conclusions and recommendations for further work are presented in Section IX..

II. Visual Snake Navigation Sensor

A. Visual Relative Motion Sensing

A critical technology for autonomous air refueling is a sensor for measuring the relative position and orientation between the receiver aircraft and the tanker aircraft. Because rapid control corrections are required for docking, especially in turbulence, the navigation sensor must provide accurate, high-frequency updates. The proposed autonomous refueling method uses color statistical pressure snakes^{33,32,34} to sense the relative position of the target aircraft with respect to the tanker. Statistical pressure snakes methods, or more simply visual snakes, segment the target area of the image and track the target with a closed, non-intersecting contour. Hardware experiments verify that visual snakes can provide relative position measurements at rates of 30 Hz even using a standard, off-the-shelf 800 MHz processor.³⁵ The visual snake provides not only information about the target size and centroid location, but also provides some information about the target shape through the principal axes lengths. The proposed relative motion sensor employs a simple, rear-facing camera mounted on the tanker, while the receiving vehicle has a visual target painted on its nose cone near the refueling port (see Fig. 1). Because the nominal relative position between the aircraft during a refueling maneuver is fixed, the relative heading and range to the receiver aircraft is accurately determined from the target image center of mass and principal axes sizes.

B. Visual Snake Algorithm

In 1987 Kass *et al.* proposed the original active deformable model to track targets within an images stream.³⁶ Also referred to as a visual pressure snake, the parametric curve is of the form

$$S(u) = I(x(u), y(u))', \quad u = [0, 1] \quad (1)$$

where I is the stored image, x and y are the image contour coordinates, and u is the independent curve parameter. This curve is placed into an image-gradient-derived potential field and allowed to change its shape and position in order to minimize the energy E along the length of the curve $S(u)$. The energy function is expressed as:³⁶

$$E = \int_0^1 [E_{\text{int}}(S(u)) + E_{\text{img}}(S(u), I)] du \quad (2)$$

where E_{int} is the internal energy defined as

$$E_{\text{int}} = \frac{\alpha}{2} \left| \frac{\partial}{\partial u} S(u) \right|^2 + \frac{\beta}{2} \left| \frac{\partial^2}{\partial u^2} S(u) \right|^2 du \quad (3)$$

and E_{img} is the image pressure function. The free weighting parameters α and β enforce tension and curvature requirements of the curve $S(u)$.

The active deformable models can be divided into two groups:³⁷ parametric models (snakes)^{36,33} and level-set models (geometric contours).³⁸ The original Kass snake formulation is a parametric snake solution. However, it is very difficult to tune and has several well documented limitations. For example, the target contours tend to implode in the presence of weak gradients. While level set models show excellent segmentation and robustness capabilities, they remain challenging to implement in real-time applications. Instead, this work will use modified parametric snake formulations proposed by Ivins and Porrill.³⁹ Here a pressure function is introduced which computes the statistical similarity of pixel values around a control point to create a pressure force which drives the snake toward the target boundaries. The new energy function is given by

$$E = \int_0^1 [E_{\text{int}}(S(u)) + E_{\text{img}}(S(u))] du \quad (4)$$

where the image pressure energy function E_{img} is

$$E_{\text{img}} = \rho (\partial S / \partial u)^\perp (\epsilon - 1) \quad (5)$$

and ϵ is statistical error measure of the curve $S(u)$ covering the target. Perrin and Smith suggest to replace the E_{int} expression with a single term that maintains a constant third derivative.³³ This simplified formulation includes an even snake point spacing constraint.

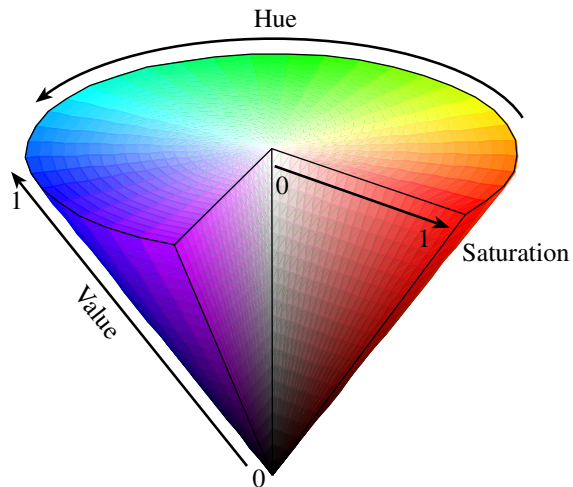


Figure 4: Conic Illustration of the Hue-Saturation-Value (HSV) Color Space.

The resulting algorithm does not contain the difficult to tune tension and curvature forces terms, yielding an easier to use and more efficient parametric snake algorithm.

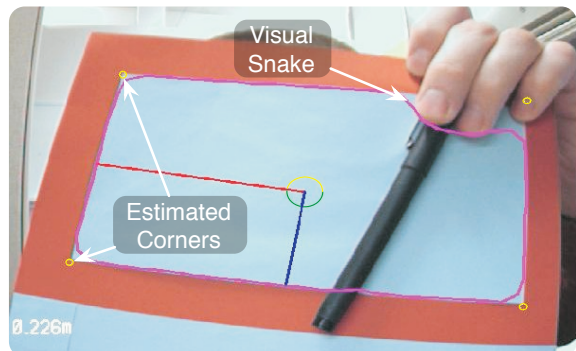
Numerical efficiency is critical when trying to apply visual snakes to the control of autonomous vehicles. A fast snake point cross-over check algorithm is implemented, which yields significant speed improvements for larger sets of snake points.³⁴ Further, to provide robustness to lighting variations, Schaub and Smith propose a new image error function:³²

$$\epsilon = \sqrt{\left(\frac{p_1 - \tau_1}{k_1 \sigma_1}\right)^2 + \left(\frac{p_2 - \tau_2}{k_2 \sigma_2}\right)^2 + \left(\frac{p_3 - \tau_3}{k_3 \sigma_3}\right)^2}$$

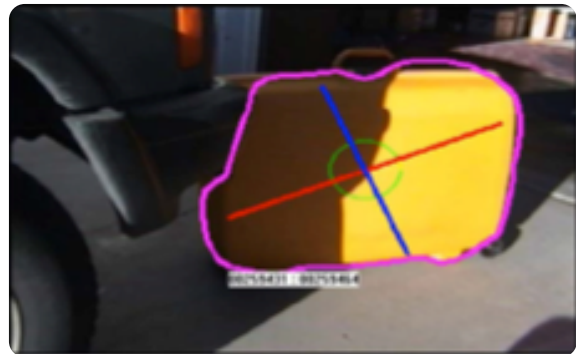
where p_i are local average pixel color channel values, τ_i are the target color channel values and σ_i are the target color channel standard deviations. The gains k_i are free to be chosen. The image RGB colors are mapped into the Hue-Saturation-Value color space illustrated in Fig. 4. By choosing appropriate gains k_i , the visual snake can track targets with significant variations in target saturation and shading.

In Reference 32 target definition enhancements are performed to move beyond the typical grey-scale definitions to utilize the full three-dimensional color space as illustrated in Fig. 5. Note the robustness of this prototype algorithm to drastic changes in lighting variations. Here the same algorithm and gains are used to track the indoor square target, as well as an outdoor yellow suitcase. The visual snake forms a closed contour about the target and is not disturbed by the presence of the black pen in Fig. 5(a). The computational requirement of the statistical snakes is relatively low compared to conventional image processing techniques such as image eigenvalue analysis. Real-time 30 Hz image processing is feasible with a 800 MHz processor without additional hardware acceleration. The computational efficiency of the visual tracking algorithm determines the performance and control bandwidth of the relative motion tracking solution.

Using the hue-saturation-value (HSV) color space in particular, robust tracking results were demonstrated in hardware by varying lighting conditions. Fig. 5(b) illustrates how an operator is able to click on the yellow suitcase in the image, and the visual snake is able to track it. Besides computing the target centroid location, the image principle axes can be computed from the 2nd area moments and be used to track the camera rotation about its bore-sight. By defining the statistical target color properties in HSV space, the harsh shadow being cast across the target does not confuse the visual snake. This example illustrates the exciting potential of using this visual sensing method in space where dramatic lighting conditions exist. For the autonomous aircraft refueling application, a visual target is painted on the front of the aircraft. As the fueling rod is extended, the fuel docking port heading and distance of the chaser aircraft is sensed by employing the visual snake algorithm.



a) Visual Snake Tracking Partially Obscured Square Target and Estimating Corner Locations⁴⁰



b) Visual Snake Tracking Yellow Suit-Case Outdoors with Severe Lighting Variations³²

Figure 5: Examples of the Identical Visual Snake Algorithm Tracking Different Targets. Each target is selected by double-clicking on it within the image.

C. Visual Snake Performance

This section discusses the performance of the visual snake algorithm as a relative navigation sensing technique. The accuracy of this sensing method is determined primarily by the accuracy of the target area, COM, and principal axis length measurements. We therefore seek to compare the measured values for these parameters with the true values. However, determining the true values in real world test conditions is extremely challenging. Moreover, due to issues related to target colors, pixelation at the target image boundary, and lens distortion specific to a particular camera/lens system, the performance would only be indicative of a particular test case, rather than the algorithm as a whole. We therefore confine this discussion to an ideal test case that shows the performance of the algorithm itself. This ideal test case represents an upper bound of the best achievable performance of the snake algorithm as a visual sensor.

To construct the ideal test case, a “perfect” target of known size, shape, location, and pure color is drawn on the video image frame before processing with the visual snake. An example frame shot at high magnification is seen in Figure 6. Note the perfectly crisp color boundaries in the ideal test image, in contrast to the boundaries seen in an image taken with a real camera. Performance data is taken for a rectangular target with a width of 200 pixels. The visual snake is started 20 times and a total of 5000 image frames are captured. The transients associated with the snake first converging to the target are removed, so the remaining data represents “steady-state” performance.

First, note that the COM and principal axis length measurement errors resulting from the visual snake are approximately Gaussian, as seen in Figure 7. This implies that combining the visual snake with a Kalman filter might enhance the accuracy of the measurements. However, in this initial proof-of-concept study such Kalman filters have not been implemented. Rather, very simple gaussian error models are used to evaluate the basic concept. Future research will develop a simulation environment where an image stream can be processed by the visual snake algorithm. Such a simulation will

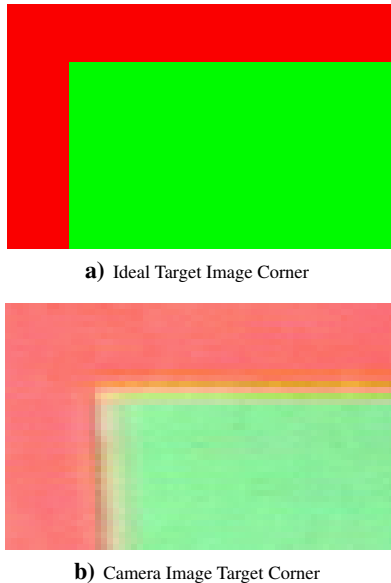


Figure 6: Zoomed View of Target Edge for Ideal Test Image and Camera Image.

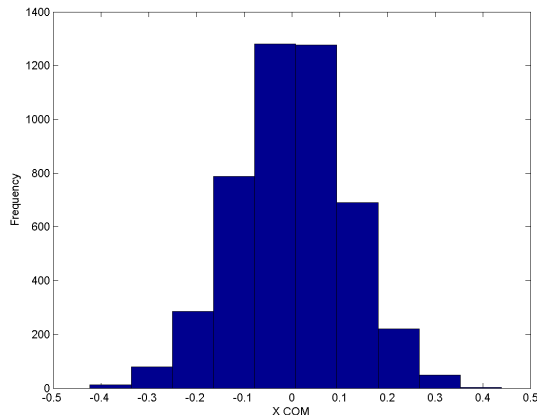


Figure 7: Histogram of X COM Measurement Error from Visual Snake Algorithm with Elliptical Ideal Test Image.

Table 1: Statistically Averaged Snake Performance for an Elliptical Target of Size 200 Pixels

Description	Pixels	Percentage
σ_{COM_x}	0.1088	0.0544%
σ_{Length}	0.1347	0.0674%

account for image blurring and degradation effects. Also, trade-off studies for ideal target to camera focal length and pixel density will need to be performed.

In air refueling problem where the vehicle attempts to maintain a constant range and orientation to a target, the visual snake can be “calibrated” about this nominal state, and better performance can be obtained. Table 1 shows the performance for a rectangular target at an image size of 200 pixels. The bias errors are corrected so that the mean values match the true values for this image size. The values in Table 1 represent an upper-bound on the best expected performance of this visual snake algorithm as a relative position sensor. When implemented in the following numerical simulations, these error levels are multiplied by a factor of 2 to account of some level of additional image sensor errors.

D. Target Setup using Perspective Projection

To use visual snakes as part of an air refueling system, a camera and a visual target must be placed on the tanker and receiver

aircraft, respectively. The visual target should be placed as close as possible to the receiver aircraft receptacle. This greatly reduces any position errors that might be introduced by the inability of the visual snake sensor to measure the full 3 DOF orientation of the receiver aircraft.

The target image COM location is used to determine the 2D relative heading to the target, and the principal axis sizes are used to determine range. From these measurements, the relative position of the receptacle is determined. For particular target shapes, the principal axis sizes are determined from the target image moments. However, when using the target area, first, and second moments, this only holds for target shapes parameterizable by two measurements and for which there is an analytical relationship between those parameters and the moments. Examples include a rectangle, which is parameterized by its length and width, or an ellipse, parameterized by its semi-major and semi-minor axes. For an arbitrary target shape however, the relationship cannot be determined. Therefore, the target image should appear as a rectangle or an ellipse in the camera image plane.

However in general, the camera image plane is not parallel to the plane on which the visual target is drawn, which means that the target image appears skewed in the camera plane. For example, a rectangle painted on the aircraft appears as a trapezoid in the camera image plane. Moreover, it is not guaranteed that a planar surface can be found in proximity to the refueling receptacle. Therefore, simply painting a visual target of the desired shape on the aircraft is not a feasible solution.

To make the target image, which is painted on a curved surface, appear as a desired shape in the camera image plane, we suggest using perspective projection. This technique consists of painting the target image so that it appears “correct” from some desired viewing position and orientation. This is illustrated in Figure 8. It is noted that the image is only correct when viewed from the nominal pose (Fig. 8(b)), and it appears skewed when viewed from any other pose (Fig. 8(a)). However, in this air refueling application, this is not a significant problem because the air refueling operation can only take place when the aircraft are at or very near their nominal positions. The visual snake measurement errors caused by slight deviations from the nominal relative pose between the aircraft are analyzed and discussed in Section E..

To find the shape that must be painted on the target to produce the desired camera image plane shape, rays are projected from the desired image shape on the camera plane through the focal point. The intersection of those rays and the receiver aircraft surface generates the contour that appears as the desired shape in the camera image plane.

E. Sensitivity Analysis

As discussed in the previous section, the use of perspective projection implies that the target image is only the “correct” shape when the relative pose between the aircraft is the nominal pose. Perturbations from the nominal pose skew the target image shape, and the resulting moments calculated from the snake contour change. The relative COM heading and range calculations are therefore corrupted when there are perturbations from the nominal pose.

A numerical simulation designed to identify the error between the visual snake-measured and true relative headings and ranges is developed. This simulation assumes that the visual target is coincident with the refueling receptacle. For this analysis, the visual snake is assumed to track the target perfectly. The calculated errors are due to the method of extracting the relative heading and range from a contour, not the visual snake tracking errors. Using this simulation, the sensitivity of the relative heading and range errors to small perturbations about the nominal position and orientation of the receiver aircraft are determined with finite-difference derivatives.

Tables 2 and 3 show the error sensitivity to position and orientation perturbations, respectively. Standard aircraft coordinate systems (X forward, Y toward the right wing, Z down) and 3-2-1 (yaw, pitch, roll) Euler Angles are used. The nominal range between the camera and the visual target is 10.7 m. Because the visual snake measurement error is not included, these values are

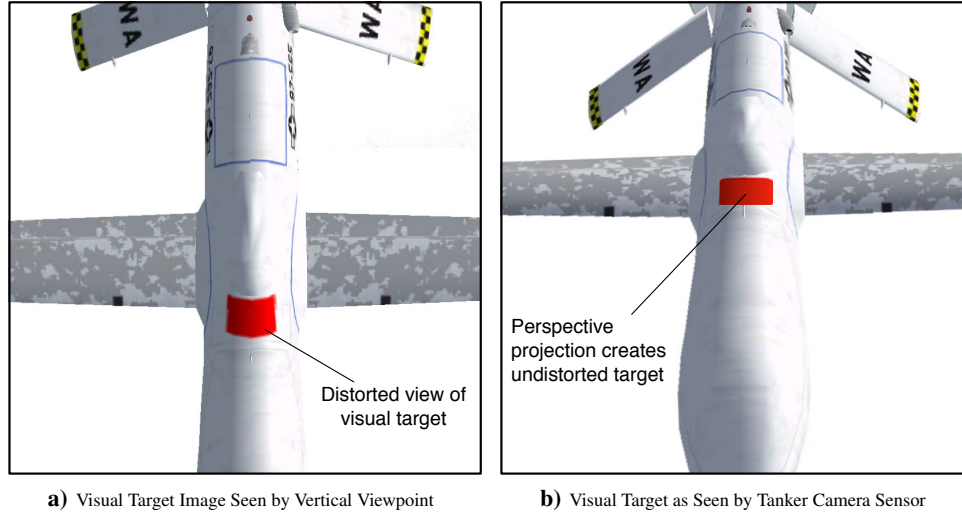


Figure 8: Illustration of Perspective Projection Showing the Visual Target from Two Different Viewpoints.

the sensitivity of the algorithm itself, and represent an upper bound on the performance of the entire visual sensing method.

Table 2: Range Error and Heading Error Sensitivity to Perturbations from Nominal Position, Visual Position Sensing Simulation

Axis	Range Error Sensitivity (m/m)	Heading Error Sensitivity (deg./m)
X	0.8756	0.0569
Y	0.0169	0.0009
Z	-0.5232	0.0372

In Table 2, the sensitivities to Y position perturbations are much lower than the other axes. This is because the nominal position is assumed to be directly in line with the tanker aircraft. In Table 3, perturbations in pitch are seen to be strongly coupled with range errors, while roll and yaw perturbations are strongly coupled with heading errors.

Table 3: Range Error and Heading Error Sensitivity to Perturbations from Nominal Orientation, Visual Position Sensing Simulation

Angle	Range Error Sensitivity (m/deg.)	Heading Error Sensitivity (deg./deg.)
Yaw	0.0011	0.1606
Pitch	-0.1228	0.0460
Roll	4.761×10^{-4}	0.1405

F. Visual Snake Sensor Simulation Results

This example shows the accuracy with which the visual snake can determine the 3D position of the receiver aircraft in favorable conditions, and is designed to show an upper limit on the sensor performance. The visual snake tracking errors are introduced to the numerical aircraft relative motion simulation to emulate the true performance of the visual sensing system. These simulations assume the receiver aircraft is at the nominal position, and, therefore do not include the effects of wind gusts, controls, *etc.*

The snake COM and principal axes size measurements are corrupted with Gaussian noise according to the characteristics deter-

Table 4: Error Magnitude, Range Error, and Heading Error Data, Visual Position Sensing Simulation.

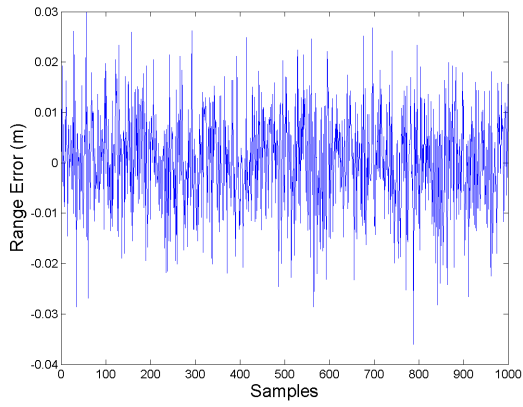
Quantity	Mean	Standard Deviation
Error Magnitude (m)	0.0124	0.0057
Range Error (m)	6.2919×10^{-5}	0.0103
Heading Error (deg.)	0.0037	0.0020
Position Error from Heading Uncertainty (m)	6.89×10^{-4}	3.72×10^{-4}

mined in Section C.. Because those values represent an ideal case where the target has perfectly crisp edges and pure colors, the noise levels are multiplied by a factor of two. This helps account for the non-crisp edges generated with real cameras, as seen in Figure 6(b). These simulation results all assume that the aircraft are at the nominal relative orientation and range of 10.7 m. If this were not the case, these results would be further corrupted according to the sensitivities seen in Tables 2 and 3.

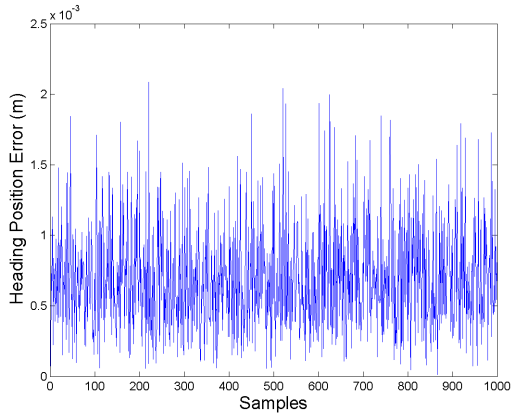
Figure 9 shows the errors resolved in the range and heading directions (with the angular heading uncertainty converted to a position uncertainty). Table 4 shows the mean and standard deviations. The error in range greatly dominates the error in heading. In other words, this visual sensing method determines the target COM heading much more accurately than it determines the range to the target. The resulting “measurement error envelope” looks like a long thin tube, as illustrated in Figure 10. The green lines represent the cone defined by the heading uncertainty, and the red region corresponds to the depth uncertainty. Both regions are exaggerated for illustration.

III. Reference Frames

The reference frames are selected as follows. The coordinate system for the tanker X_T, Y_T, Z_T , receiver X_R, Y_R, Z_R , refueling boom X_b, Y_b, Z_b are shown in Figure 11, along with the inertial coordinate system X_I, Y_I, Z_I . The origin of the tanker and receiver reference frames is located at the center of gravity (c.g.) for each vehicle. The joint of the refueling boom is the origin for the boom coordinates, and \mathbf{r}_b defines the position of the refueling boom joint from the tanker c.g. The vector \mathbf{r}_c denotes the position of the camera located at the rear of the tanker, relative to the tanker c.g. \mathbf{r}_T , \mathbf{r}_R , and \mathbf{r}_{box} are vectors referenced from the inertial coordinates to the tanker c.g., receiver c.g., and the center of the receiver’s 3D refueling box, respectively. The refueling box shown in Figure 11 is not to scale. However, the dimensions used in the simulations are based upon data from Ref. 24, and are modified slightly to the values $x \pm 0.25\text{m}$, $y \pm 0.75$, $z \pm 0.5\text{m}$.



a) Range Error



b) Position Error from Heading Uncertainty

Figure 9: Range Error, Heading Error, and Heading Position Error, Visual Position Sensing Simulation.



Figure 10: Illustration of Range Shape (red) and Heading Errors (green), Visual Position Sensing Simulation

IV. Refueling Boom Dynamical Model

The refueling boom is modeled as two rigid bodies as shown in Figure 12. One rigid body 8.4 meters long (L_1), is attached to the tanker at one end by a joint with two angular degrees-of-freedom, θ_b and ψ_b . On the free end of this fixed rigid body (L_2) are mounted two control effectors in the form of ruddervators. The ruddervators are mounted to the boom with constant dihedral angle ϕ_b and are controlled with commanded deflections δ_{b_1} and δ_{b_2} , defined as positive for trailing-edge down. The ruddervators are attached to the tanker aircraft with linkages such that their deflection angles are commanded relative to the tanker reference frame, and not the boom reference frame. The ruddervators are modeled as NACA-0012 symmetrical airfoils. The second rigid body, 8.2 meters long (L_3), is attached to the fixed rigid body by a telescoping joint with a single translational degree-of-freedom. On the free

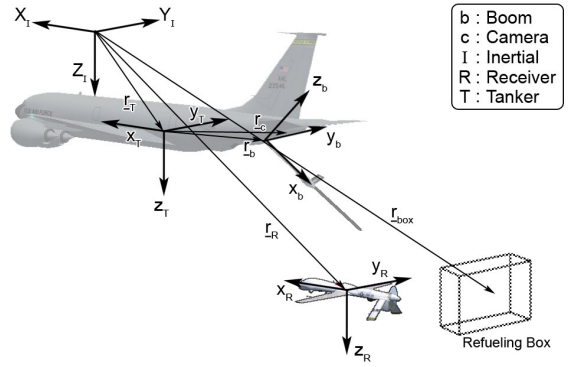


Figure 11: Reference Frames

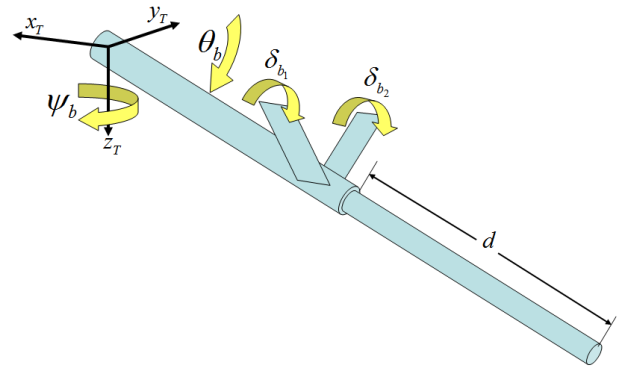


Figure 12: Refueling Boom Model External Physical Characteristics and Dimensions

end of this body (L_4) is the fuel nozzle for docking and fueling. The telescoping body can fully retract into the fixed body, and can extend a distance d outside the fixed body, up to 6.1 meters maximum.

Approximate dimensions and masses were taken from Ref. 41. The fixed rigid body is modeled as a thin rod with a distributed mass m_1 , plus a point mass m_2 located near the end of the body where the pod housing the aerodynamic control mechanism is mounted. The telescoping rigid body is modeled similarly, as a thin rod with distributed mass m_3 and a point mass m_4 for the nozzle and docking assembly at the end of the body. The nonlinear equations of motion for the boom system were derived assuming no coupling between the boom and the tanker aircraft. These equations of motion were linearized to obtain the dynamical model of the boom used in this paper. Since the boom model parameters change slowly, and the amplitude of linear displacements, angular displacements, and velocities for boom operation is small, linear time-invariant (LTI) models are derived. In the equations, g is the constant gravitational acceleration and \bar{q} is the dynamic pressure at the nominal airspeed. Additionally, C_{l_α} and C_{d_α} are the change in lift and drag coefficients due to change in angle-of-attack for the ruddervators, while C_{d_b} is the drag coefficient for the boom cross-section. The parameter S represents the surface area of one of the ruddervators, while I and W_b are related to the inertia and weight of the boom, respectively. The numerical values of the model parameters are listed in the Appendix. The 1 subscript on variables $I, d, \theta, \delta_{b_1}, \delta_{b_2}$ represent the steady-state values of these variables.

$$A_{b1} = [L_2(\cos \phi \sin \theta_1 C_{l_\alpha} \bar{q} S(\delta_{b_{11}} + \delta_{b_{21}}) - \cos \theta_1 (C_{d_b} \bar{q} (L_1 + d_1) + \bar{q} S(2C_{d_0} + C_{d_\alpha} (|\delta_{b_{11}}| + |\delta_{b_{21}}|))) - g \sin \theta_1 (d_1 (m_3 + m_4) + W_b)]/I_1 \quad (6)$$

$$A_{b2} = (-L_2 \sin \theta_1 C_{d_b} \bar{q} - g \sin \theta_1 (m_3 + m_4))/I_1 \quad (7)$$

$$B_{b1} = -L_2 \bar{q} S(\sin \theta_1 C_{d_\alpha} + \cos \phi \cos \theta_1 C_{l_\alpha})/I_1 \quad (8)$$

$$B_{b2} = (L_2 \sin \phi C_{l_\alpha} \bar{q} S)/(I_1 \cos \theta_1) \quad (9)$$

$$I_1 = m_1 L_1^2/3 + m_2 L_2^2 + m_3 (d_1^2 + d_1 L_3 + L_3^2/3) + m_4 (d_1^2 + 2d_1 L_4 + L_4^2) \quad (10)$$

$$W_b = m_1 L_1/2 + m_2 L_2 + m_3 L_3/2 + m_4 L_4 \quad (11)$$

These linear equations of motion are converted to the state-space form

$$\dot{\mathbf{x}} = \mathbf{A}\mathbf{x} + \mathbf{B}\mathbf{u} \quad (12)$$

with state vector $\mathbf{x} \in \mathbb{R}^n$, control vector $\mathbf{u} \in \mathbb{R}^m$, plant matrix $\mathbf{A} \in \mathbb{R}^{n \times n}$, and control distribution matrix $\mathbf{B} \in \mathbb{R}^{n \times m}$, where n is the number of states, and m is the number of controls. This conversion results in

$$\begin{bmatrix} \dot{\theta} \\ \ddot{\theta} \\ \dot{\psi} \\ \ddot{\psi} \\ \dot{d} \\ \ddot{d} \end{bmatrix} = \begin{bmatrix} 0 & 1 & 0 & 0 & 0 & 0 \\ A_{b1} & 0 & 0 & 0 & A_{b2} & 0 \\ 0 & 0 & 0 & 1 & 0 & 0 \\ 0 & 0 & 0 & 0 & 0 & 0 \\ 0 & 0 & 0 & 0 & 0 & 1 \\ 0 & 0 & 0 & 0 & 0 & 0 \end{bmatrix} \begin{bmatrix} \theta \\ \dot{\theta} \\ \psi \\ \dot{\psi} \\ d \\ \dot{d} \end{bmatrix} + \begin{bmatrix} 0 & 0 & 0 \\ B_{b1} & B_{b1} & 0 \\ 0 & 0 & 0 \\ -B_{b2} & B_{b2} & 0 \\ 0 & 0 & 0 \\ 0 & 0 & 1 \end{bmatrix} \begin{bmatrix} \delta_{b1} \\ \delta_{b2} \\ \delta_d \end{bmatrix} \quad (13)$$

The state-space linear model of the refueling boom containing numerical values is presented in the Appendix.

V. Receiver and Tanker Aircraft Dynamical Models

The receiver and tanker aircraft dynamical models are expressed in the stability axis system, as defined in Figure 13. Here X_b, Y_b, Z_b are the longitudinal, lateral, and directional axes of the body-fixed coordinate system whose origin is fixed at the center of mass, α is the angle-of-attack, β is the sideslip angle, and V_{res} is the velocity vector.

For the air refueling maneuvers considered here, both the receiver aircraft and the tanker aircraft remain at or near the trim condition in steady, level, 1g flight. Since the model parameters do not change quickly, and the amplitude of linear displacements, angular displacements, and velocities for these maneuvers are small, LTI models are derived. Considering both the longitudinal and lateral/directional dynamics, the linear equations of motion of this coupled system about a trim point are derived assuming that steady-state pitch rate, roll rate, and yaw rate are equal to zero ($P_1 = Q_1 = R_1 = 0$); body axis side-velocity and vertical velocity are equal to zero ($V_1 = W_1 = 0$), and pitch attitude angle Θ_1 and bank angle Φ_1 are both constant. The resulting LTI equations of motion in the stability-axis system are:

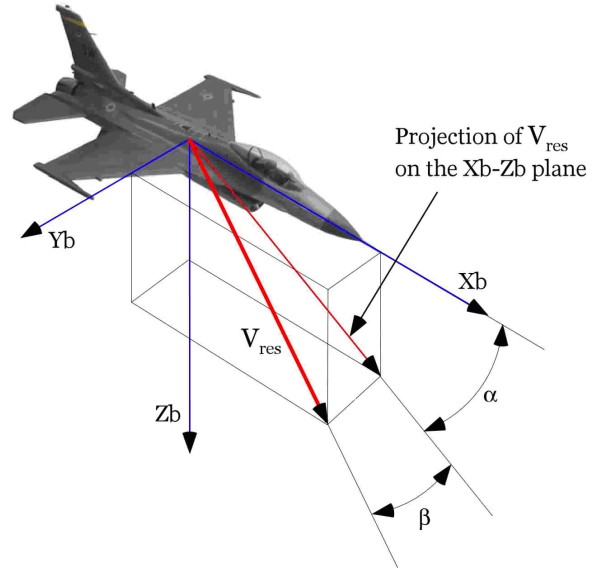


Figure 13: Body Axis Systems and Definition of Aerodynamic Angles

$$\begin{aligned} \dot{u} &= -g\theta \cos \Theta_1 + (X_{T_u} + X_u)u + X_\alpha \alpha + X_q q \\ &\quad + X_{\delta_e} \delta_e + X_{\delta_T} \delta_T + X_{\dot{\alpha}} \dot{\alpha} \\ \dot{\alpha} &= (-g\theta \sin \Theta_1 \cos \Phi_1 + Z_u u + Z_\alpha \alpha + Z_q q + U_1 q \\ &\quad + Z_{\delta_e} \delta_e + Z_{\delta_T} \delta_T + Z_{\dot{\alpha}} \dot{\alpha} - g\phi \cos \Theta_1 \sin \Phi_1)/U_1 \\ \dot{q} &= (M_{T_u} + M_u)u + (M_{T_\alpha} + M_\alpha)\alpha + M_q q + M_{\delta_e} \delta_e \\ &\quad + M_{\delta_T} \delta_T + M_{\dot{\alpha}} \dot{\alpha} \\ \dot{\theta} &= q \cos \Phi_1 - r \sin \Phi_1 \\ \dot{\beta} &= (Y_p p + g\phi \cos \Theta_1 \cos \Phi_1 + g\theta \sin \Theta_1 \sin \Phi_1 \\ &\quad + Y_\beta \beta + (Y_r - U_1)r + Y_{\delta_A} \delta_A + Y_{\delta_R} \delta_R)/U_1 \\ \dot{p} &= L_\beta \beta + L_p p + L_r r + L_{\delta_A} \delta_A + L_{\delta_R} \delta_R + \frac{I_{xz}}{I_{xx}} \dot{r} \\ \dot{r} &= N_\beta \beta + N_p p + N_r r + N_{\delta_A} \delta_A + N_{\delta_R} \delta_R + \frac{I_{xz}}{I_{zz}} \dot{p} \\ \dot{\phi} &= p + r \cos \Phi_1 \tan \Theta_1 + q \sin \Phi_1 \tan \Theta_1 \\ \dot{\psi} &= r \cos \Phi_1 \sec \Theta_1 + q \sin \Phi_1 \sec \Theta_1 \end{aligned} \quad (14)$$

In Eq.14 U_1 is the trim airspeed, the I are the moments and products of inertia, and g is the gravitational constant. The independent variables are perturbed total velocity u ; roll, pitch, and yaw angular velocities p, q, r ; kinematic roll, pitch, and yaw angles ϕ, θ, ψ ; angle-of-attack α ; and sideslip angle β . The controls are perturbed elevator deflection δ_e ; perturbed aileron deflection δ_a ; perturbed rudder deflection δ_r ; and perturbed throttle position δ_T . The coefficients on the right hand side of Eq. 14 are dimensional stability derivatives, in which X, Y, Z are the longitudinal, side, and vertical forces; and L, M, N are the roll, pitch, and yaw moments. Each dimensional stability derivative corresponds to a specific non-dimensional stability derivative, and represents the translational or angular acceleration imparted to the system due to a perturbation in the subscripted state variable or control variable. For example, M_α is a function of C_{m_α} and represents the pitch angular acceleration imparted to the system due to a perturbation in angle-of-attack. Likewise, Y_{δ_r} is a function of $C_{y_{\delta_r}}$, and represents the side translational acceleration due to a perturbation in rudder deflection.

To obtain a state-space representation of Eq.14, it is cast into the form

$$E\dot{\mathbf{x}} = \mathbf{A}\mathbf{x} + \mathbf{B}\mathbf{u} \quad (15)$$

with state vector $\mathbf{x} \in \mathbb{R}^n$, control vector $\mathbf{u} \in \mathbb{R}^m$, mass matrix $E \in \mathbb{R}^{n \times n}$, plant matrix $\mathbf{A} \in \mathbb{R}^{n \times n}$, and control distribution matrix $\mathbf{B} \in \mathbb{R}^{n \times m}$, where n is the number of states, and m is the number of controls. Defining the state vector as

$$\mathbf{x} = [u \quad \alpha \quad q \quad \theta \quad \beta \quad p \quad r \quad \phi \quad \psi]^T \quad (16)$$

and the control vector as

$$\mathbf{u} = [\delta_e \quad \delta_T \quad \delta_a \quad \delta_r]^T \quad (17)$$

the mass matrix will then have the form

$$E = \begin{bmatrix} 1 & -X_{\dot{\alpha}} & 0 & 0 & 0 & 0 & 0 & 0 & 0 \\ 0 & 1 - \frac{Z_{\dot{\alpha}}}{U_1} & 0 & 0 & 0 & 0 & 0 & 0 & 0 \\ 0 & -M_{\dot{\alpha}} & 1 & 0 & 0 & 0 & 0 & 0 & 0 \\ 0 & 0 & 0 & 1 & 0 & 0 & 0 & 0 & 0 \\ 0 & 0 & 0 & 0 & 1 & 0 & 0 & 0 & 0 \\ 0 & 0 & 0 & 0 & 0 & 1 & -\frac{I_{xz}}{I_{xx}} & 0 & 0 \\ 0 & 0 & 0 & 0 & 0 & -\frac{I_{xz}}{I_{zz}} & 1 & 0 & 0 \\ 0 & 0 & 0 & 0 & 0 & 0 & 0 & 1 & 0 \\ 0 & 0 & 0 & 0 & 0 & 0 & 0 & 0 & 1 \end{bmatrix} \quad (18)$$

Multiplying both sides of Eq. 15 by E^{-1} produces the desired form

$$\dot{\mathbf{x}} = E^{-1}A\mathbf{x} + E^{-1}B\mathbf{u} \quad (19)$$

in which

$$E^{-1}A = \begin{bmatrix} X'_u & X'_\alpha & X'_q & X'_\theta & 0 & \dots \\ Z'_u & Z'_\alpha & Z'_q & Z'_\theta & 0 & \dots \\ M'_u & M'_\alpha & M'_q & M'_\theta & 0 & \dots \\ 0 & 0 & \cos \Phi_1 & 0 & -\sin \Phi_1 & \dots \\ 0 & 0 & 0 & \frac{Y_\theta}{U_1} & \frac{Y_\beta}{U_1} & \dots \\ 0 & 0 & 0 & 0 & L'_\beta & \dots \\ 0 & 0 & 0 & 0 & N'_\beta & \dots \\ 0 & 0 & \sin \Phi_1 \tan \Theta_1 & 0 & 0 & \dots \\ 0 & 0 & \sin \Phi_1 \sec \Theta_1 & 0 & 0 & \dots \\ \dots & 0 & 0 & 0 & 0 & \dots \\ \dots & 0 & Z'_\phi & 0 & 0 & \dots \\ \dots & 0 & 0 & 0 & 0 & \dots \\ \dots & 0 & 0 & 0 & 0 & \dots \\ \dots & \frac{Y_p}{U_1} & \left(\frac{Y_r}{U_1} - 1\right) & \frac{g \cos \Theta_1}{U_1} & 0 & \dots \\ \dots & L'_p & L'_r & 0 & 0 & \dots \\ \dots & N'_p & N'_r & 0 & 0 & \dots \\ \dots & 1 & \cos \Phi_1 \tan \Theta_1 & 0 & 0 & \dots \\ \dots & 0 & 0 & \cos \Phi_1 \sec \Theta_1 & 0 & \dots \end{bmatrix} \quad (20)$$

and

$$E^{-1}B = \begin{bmatrix} X'_{\delta_e} & X'_{\delta_T} & 0 & 0 \\ Z'_{\delta_e} & Z'_{\delta_T} & 0 & 0 \\ M'_{\delta_e} & M'_{\delta_T} & 0 & 0 \\ 0 & 0 & 0 & 0 \\ 0 & 0 & \frac{Y_{\delta_A}}{U_1} & \frac{Y_{\delta_R}}{U_1} \\ 0 & 0 & L'_{\delta_A} & L'_{\delta_R} \\ 0 & 0 & N'_{\delta_A} & N'_{\delta_R} \\ 0 & 0 & 0 & 0 \\ 0 & 0 & 0 & 0 \end{bmatrix} \quad (21)$$

The primed quantities in Eq. 20 and Eq. 21 result from the elimination of the $\dot{\alpha}$, \dot{p} , and \dot{r} terms in the lift, roll rate, and yaw rate equations respectively, due to the operation Eq. 19.

Assembling Eq.20 - Eq. 21 results in the state-space model

$$\begin{bmatrix} \dot{u} \\ \dot{\alpha} \\ \dot{q} \\ \dot{\theta} \\ \dot{\beta} \\ \dot{p} \\ \dot{r} \\ \dot{\phi} \\ \dot{\psi} \end{bmatrix} = \begin{bmatrix} X'_u & X'_\alpha & X'_q & X'_\theta & 0 & \dots \\ Z'_u & Z'_\alpha & Z'_q & Z'_\theta & 0 & \dots \\ M'_u & M'_\alpha & M'_q & M'_\theta & 0 & \dots \\ 0 & 0 & \cos \Phi_1 & 0 & -\sin \Phi_1 & \dots \\ 0 & 0 & 0 & \frac{Y_\theta}{U_1} & \frac{Y_\beta}{U_1} & \dots \\ 0 & 0 & 0 & 0 & L'_\beta & \dots \\ 0 & 0 & 0 & 0 & N'_\beta & \dots \\ 0 & 0 & \sin \Phi_1 \tan \Theta_1 & 0 & 0 & \dots \\ 0 & 0 & \sin \Phi_1 \sec \Theta_1 & 0 & 0 & \dots \\ \dots & 0 & 0 & 0 & 0 & \dots \\ \dots & 0 & Z'_\phi & 0 & 0 & \dots \\ \dots & 0 & 0 & 0 & 0 & \dots \\ \dots & 0 & 0 & 0 & 0 & \dots \\ \dots & \frac{Y_p}{U_1} & \left(\frac{Y_r}{U_1} - 1\right) & \frac{g \cos \Theta_1}{U_1} & 0 & \dots \\ \dots & L'_p & L'_r & 0 & 0 & \dots \\ \dots & N'_p & N'_r & 0 & 0 & \dots \\ \dots & 1 & \cos \Phi_1 \tan \Theta_1 & 0 & 0 & \dots \\ \dots & 0 & 0 & \cos \Phi_1 \sec \Theta_1 & 0 & \dots \end{bmatrix} \begin{bmatrix} u \\ \alpha \\ q \\ \theta \\ \beta \\ p \\ r \\ \phi \\ \psi \end{bmatrix} +$$

$$\begin{bmatrix} X'_{\delta_e} & X'_{\delta_T} & 0 & 0 \\ Z'_{\delta_e} & Z'_{\delta_T} & 0 & 0 \\ M'_{\delta_e} & M'_{\delta_T} & 0 & 0 \\ 0 & 0 & 0 & 0 \\ 0 & 0 & \frac{Y_{\delta_A}}{U_1} & \frac{Y_{\delta_R}}{U_1} \\ 0 & 0 & L'_{\delta_A} & L'_{\delta_R} \\ 0 & 0 & N'_{\delta_A} & N'_{\delta_R} \\ 0 & 0 & 0 & 0 \end{bmatrix} \begin{bmatrix} \delta_e \\ \delta_T \\ \delta_a \\ \delta_r \end{bmatrix} \quad (22)$$

Eq. 22 applies to both the receiver aircraft and the tanker aircraft, and numerical values for the elements are determined using USAF Data Compendium (DATCOM) methods.⁴² The non-parametric linear models of the tanker and receiver aircraft used for controller synthesis and for simulation are provided in the Appendix. The receiver aircraft model used for controller design and simulation purposes is called UCAV6, a roughly 60% scale AV-8B Harrier aircraft, with the pilot and support devices removed and the mass properties and aerodynamics adjusted accordingly to represent a UAV. For the simulations presented here, all thrust vectoring capability is disabled. The UCAV6 longitudinal and lateral/directional linear models used for both controller synthesis and simulation in this paper were obtained from the UCAV6 nonlinear simulation.⁵ Atmospheric turbulence on the receiver UAV is modeled using the Dryden turbulence model, and the wake vortex effect from the tanker flowfield is included in the simulations.

The tanker aircraft state-space linear model uses Boeing 747 stability and control derivatives,⁴³ which are representative of large multi-engine tankers of the KC-135 and KC-10 classes. In the docking maneuvers investigated here, the initial rendezvous between tanker and receiver is assumed to have been achieved, with the receiver positioned in steady-state behind the tanker. The tanker aircraft is assumed to be flying in steady, level, 1-g straight line flight at constant velocity.

VI. Refueling Boom Docking Controller

A. Optimal Nonzero Set Point Controller

The optimal Nonzero Setpoint (NZSP) is a command structure which steers the plant from initial steady-state or trim conditions, to specified terminal trim conditions, with guaranteed tracking properties. It is used here to develop a simple yet functional baseline

autonomous boom docking controller. Consider the linear time-invariant system with n states, m controls, and p outputs:

$$\begin{aligned}\dot{\mathbf{x}} &= A\mathbf{x} + B\mathbf{u}; & \mathbf{x}(0) &= \mathbf{x}_0 \\ \mathbf{y} &= C\mathbf{x} + D\mathbf{u}\end{aligned}\quad (23)$$

with state vector $\mathbf{x} \in \mathbb{R}^n$, control vector $\mathbf{u} \in \mathbb{R}^m$, output vector $\mathbf{y} \in \mathbb{R}^p$, plant matrix $A \in \mathbb{R}^{n \times n}$, control distribution matrix $B \in \mathbb{R}^{n \times m}$, output matrix $C \in \mathbb{R}^{p \times n}$, and carry-through matrix $D \in \mathbb{R}^{p \times m}$. For synthesizing a sampled-data controller, the continuous time state-space representation is discretized for controller sample period T using the relation for the discrete state matrix Φ

$$\Phi(T) = e^{AT} \quad (24)$$

and the relation for the discrete control distribution matrix Γ

$$\Gamma = \left(\int_0^T e^{A\tau} d\tau \right) B \quad (25)$$

These relations are used to produce the discretized linear time-invariant system

$$\begin{aligned}\mathbf{x}_{k+1} &= \Phi\mathbf{x}_k + \Gamma\mathbf{u}_k \\ \mathbf{y}_k &= H\mathbf{x}_k + D\mathbf{u}_k\end{aligned}\quad (26)$$

where H and D are the discrete equivalents of the continuous matrices C and D respectively. It is desired to command certain initial steady-state outputs \mathbf{y}_k to terminal steady-state outputs \mathbf{y}_{m_k} and keep them there as $t \rightarrow \infty$. If these terminal outputs are new steady-state trim states, denoted by $*$, then at these new trim conditions the system is characterized by

$$\begin{aligned}\mathbf{x}_{k+1}^* &= \Phi\mathbf{x}_k^* + \Gamma\mathbf{u}_k^* \equiv 0 \\ \mathbf{y}_{m_k} &= H\mathbf{x}_k^* + D\mathbf{u}_k^* \\ \mathbf{x}_k^* &\in \mathbb{R}^n, \quad \mathbf{u}_k^* \in \mathbb{R}^m, \quad \mathbf{y}_{m_k} \in \mathbb{R}^p\end{aligned}\quad (27)$$

where p is the number of terminal or commanded outputs, and the subscript m on the output vector denotes a vector of commanded outputs. Error states and error controls are next defined respectively as

$$\begin{aligned}\tilde{\mathbf{x}}_k &= \mathbf{x}_k - \mathbf{x}^* \\ \tilde{\mathbf{u}}_k &= \mathbf{u}_k - \mathbf{u}^*\end{aligned}\quad (28)$$

where $\tilde{\mathbf{x}}_k$ is the error between the initial trim state and the commanded trim state, and $\tilde{\mathbf{u}}_k$ is the error between the initial control and the control at the commanded trim state. By substituting Eq. (26) and Eq. (27) into Eq. (28), the error state equation can be written as

$$\begin{aligned}\tilde{\mathbf{x}}_{k+1} &= \mathbf{x}_{k+1} - \mathbf{x}_{k+1}^* = \Phi\mathbf{x}_k + \Gamma\mathbf{u}_k - (\Phi\mathbf{x}^* + \Gamma\mathbf{u}^*) \\ \tilde{\mathbf{x}}_{k+1} &= \Phi\tilde{\mathbf{x}}_k + \Gamma\tilde{\mathbf{u}}_k\end{aligned}\quad (29)$$

with sampled-data regulator quadratic cost function to be minimized

$$J = \frac{1}{2} \sum_{n=0}^{\infty} \left[\tilde{\mathbf{x}}_n^T \hat{Q} \tilde{\mathbf{x}}_n + \tilde{\mathbf{u}}_n^T \hat{R} \tilde{\mathbf{u}}_n + 2\tilde{\mathbf{x}}_n^T M \tilde{\mathbf{u}}_n \right] \quad (30)$$

in which \hat{Q} , \hat{R} , and M are weighting matrices. The optimal control that minimizes Eq. (30) is obtained by solving for the discrete Riccati equation P using the matrix algebraic Riccati equation with infinite horizon

$$\begin{aligned}\Phi^T P_{n+1} \Phi + \hat{Q} - (\Gamma^T P_{n+1} \Phi + M^T)^T \\ (\hat{R} + \Gamma^T P_{n+1} \Phi + M^T) = 0\end{aligned}\quad (31)$$

A feedback control law in terms of the measured states is then obtained by converting the error controls $\tilde{\mathbf{u}}_k$ back to \mathbf{u}_k , giving

$$\mathbf{u}_k = (\mathbf{u}^* + K\mathbf{x}^*) - K\mathbf{x}_k \quad (32)$$

with \mathbf{u}^* and \mathbf{x}^* constants to be solved for, and gain matrix

$$K = (\hat{R} + \Gamma^T P \Gamma)^{-1} (\Gamma^T P \Phi + M^T) \quad (33)$$

Assuming the system (Φ, Γ) is controllable, the constants \mathbf{x}^* and \mathbf{u}^* are determined by first expressing Eq. (27) in vector-matrix form as

$$\begin{bmatrix} (\Phi - I) & \Gamma \\ H & D \end{bmatrix} \begin{bmatrix} \mathbf{x}^* \\ \mathbf{u}^* \end{bmatrix} = \begin{bmatrix} \mathbf{0} \\ \mathbf{y}_{m_k} \end{bmatrix} \quad (34)$$

where the system matrix is called the quad partition matrix, composed of sub-matrices $(\Phi - I) \in \mathbb{R}^{n \times n}$, $\Gamma \in \mathbb{R}^{n \times m}$, $H \in \mathbb{R}^{p \times n}$, and $D \in \mathbb{R}^{p \times m}$. Values for \mathbf{x}^* and \mathbf{u}^* are solved for according to

$$\begin{bmatrix} \mathbf{x}^* \\ \mathbf{u}^* \end{bmatrix} = \begin{bmatrix} \Pi_{11} & \Pi_{12} \\ \Pi_{21} & \Pi_{22} \end{bmatrix} \begin{bmatrix} \mathbf{0} \\ \mathbf{y}_{m_k} \end{bmatrix} \quad (35)$$

where the matrix Π is defined as the inverse of the quad partition matrix,

$$\begin{bmatrix} \Pi_{11} & \Pi_{12} \\ \Pi_{21} & \Pi_{22} \end{bmatrix} = \begin{bmatrix} (\Phi - I) & \Gamma \\ H & D \end{bmatrix}^{-1} \quad (36)$$

This is the standard inverse problem, in which there is the possibility of exactly one solution (the determined case), an infinity of solutions (the underdetermined case), or no solution (the overdetermined case).⁴⁴ Each case is briefly discussed in the context of the present problem.

For the determined case, which will produce the desired exact trajectory tracking, unique solutions for \mathbf{x}^* and \mathbf{u}^* exist only if the quad partition matrix in Eq. (36) is full rank. For a controllable system with the dimensions of the matrices $(\Phi - I)$ and Γ determined by the system characteristics, the dimensions of H and D can be selected to produce a square quad partition matrix. This dimensionality criterion is satisfied when the number of outputs selected to be tracked, p , is equal to the number of controls, m . Expanding Eq. (34) produces the desired expressions for the new trim states and controls:

$$\begin{aligned}\mathbf{x}^* &= \Pi_{12} \mathbf{y}_{m_k} \\ \mathbf{u}^* &= \Pi_{22} \mathbf{y}_{m_k}\end{aligned}\quad (37)$$

The underdetermined case, also known as the minimum norm solution, produces an infinity of exact solutions instead of a unique exact solution. It occurs when there are fewer independent equations than unknowns, which for the present problem occurs when the number of outputs selected to be tracked, p , is less than the number of controls, m . A minimum norm solution is often used for this case, which is the solution $\hat{\mathbf{x}}$ that minimizes the norm

$$\mathbf{J} = \frac{1}{2} \begin{bmatrix} \mathbf{x}^* \\ \mathbf{u}^* \end{bmatrix}^T \begin{bmatrix} \mathbf{x}^* \\ \mathbf{u}^* \end{bmatrix} \quad (38)$$

subject to Eq. (34). The analytical solution is obtained by introducing a vector of Lagrange multipliers to adjoin the constraint of Eq. 34 to Eq. 38, to produce the augmented norm

$$\mathbf{J}_{\text{aug}} = \frac{1}{2} \begin{bmatrix} \mathbf{x}^* \\ \mathbf{u}^* \end{bmatrix}^T \begin{bmatrix} \mathbf{x}^* \\ \mathbf{u}^* \end{bmatrix} + \lambda^T \left(\begin{bmatrix} \mathbf{0} \\ \mathbf{y}_{m_k} \end{bmatrix} - \begin{bmatrix} (\Phi - I) & \Gamma \\ H & D \end{bmatrix} \begin{bmatrix} \mathbf{x}^* \\ \mathbf{u}^* \end{bmatrix} \right) \quad (39)$$

Minimizing the augmented norm produces the desired minimum norm solution for \mathbf{x}^* and \mathbf{u}^* :

$$\begin{bmatrix} \hat{\mathbf{x}}^* \\ \hat{\mathbf{u}}^* \end{bmatrix} = \begin{bmatrix} (\Phi - I) & \Gamma \\ H & D \end{bmatrix}^T \left(\begin{bmatrix} (\Phi - I) & \Gamma \\ H & D \end{bmatrix} \begin{bmatrix} (\Phi - I) & \Gamma \\ H & D \end{bmatrix}^T \right)^{-1} \begin{bmatrix} \mathbf{0} \\ \mathbf{y}_{m_k} \end{bmatrix} \quad (40)$$

The overdetermined case, also known as the least squares solution, occurs when there are more independent equations than unknowns. For the present problem this occurs when the number

of outputs selected to be tracked, p , is greater than the number of controls, m . Generally no exact solution exists for this situation, so approximate solutions for \mathbf{x}^* and \mathbf{u}^* are sought. Since no one solution will satisfy all of the equations, it is not appropriate to use the equality of Eq. (34). Instead, an error vector is introduced

$$\mathbf{e} = \begin{bmatrix} \mathbf{0} \\ \mathbf{y}_{m_k} \end{bmatrix} - \begin{bmatrix} (\Phi - I) & \Gamma \\ H & D \end{bmatrix} \begin{bmatrix} \mathbf{x}^* \\ \mathbf{u}^* \end{bmatrix} \quad (41)$$

and the least squares approach is used to find the approximate solution $\hat{\mathbf{x}}$ that minimizes the sum of the squares of the components of \mathbf{e} . This is equivalent to determining the $\hat{\mathbf{x}}$ which yields the minimum of

$$\mathbf{J} = \frac{1}{2} \mathbf{e}^T \mathbf{e} = \frac{1}{2} \left(\begin{bmatrix} \mathbf{0} \\ \mathbf{y}_{m_k} \end{bmatrix} - \begin{bmatrix} (\Phi - I) & \Gamma \\ H & D \end{bmatrix} \begin{bmatrix} \mathbf{x}^* \\ \mathbf{u}^* \end{bmatrix} \right)^T \left(\begin{bmatrix} \mathbf{0} \\ \mathbf{y}_{m_k} \end{bmatrix} - \begin{bmatrix} (\Phi - I) & \Gamma \\ H & D \end{bmatrix} \begin{bmatrix} \mathbf{x}^* \\ \mathbf{u}^* \end{bmatrix} \right) \quad (42)$$

The necessary condition is that the gradient of \mathbf{J} with respect to \mathbf{x} must be equal to zero, which can be expressed compactly as

$$\begin{aligned} & \left(\begin{bmatrix} (\Phi - I) & \Gamma \\ H & D \end{bmatrix}^T \begin{bmatrix} (\Phi - I) & \Gamma \\ H & D \end{bmatrix} \right) \begin{bmatrix} \hat{\mathbf{x}} \\ \mathbf{u}^* \end{bmatrix} \\ & = \begin{bmatrix} (\Phi - I) & \Gamma \\ H & D \end{bmatrix}^T \begin{bmatrix} \mathbf{0} \\ \mathbf{y}_{m_k} \end{bmatrix} \end{aligned} \quad (43)$$

Solving Eq. (43) for \mathbf{x}^* and \mathbf{u}^* produces the minimum norm solution:

$$\begin{bmatrix} \hat{\mathbf{x}} \\ \mathbf{u}^* \end{bmatrix} = \left(\begin{bmatrix} (\Phi - I) & \Gamma \\ H & D \end{bmatrix}^T \begin{bmatrix} (\Phi - I) & \Gamma \\ H & D \end{bmatrix} \right)^{-1} \begin{bmatrix} (\Phi - I) & \Gamma \\ H & D \end{bmatrix}^T \begin{bmatrix} \mathbf{0} \\ \mathbf{y}_{m_k} \end{bmatrix} \quad (44)$$

Once solutions for \mathbf{x}^* and \mathbf{u}^* have been determined using one of the three methods presented above, substitution of the solutions into Eq. (32) produces the control law implementation equation

$$\mathbf{u}_k = (\Pi_{22} + K\Pi_{12})\mathbf{y}_{m_k} - K\mathbf{x}_k \quad (45)$$

A feature of this controller is the guarantee of perfect tracking, independent of the value of the gains provided they are stabilizing. The gains can be designed using any desired technique, whether classical or modern, and only affect the transient performance, not the guarantee of steady-state performance. Considering the user selection of outputs, a selected output to be tracked cannot be the time rate of change of a state in the model, since the system will not be controllable. The physical interpretation is that a state and its derivative cannot both be driven to nonzero constant values at the same time in steady-state.

B. Proportional-Integral-Filter Nonzero Setpoint Controller

It was assumed for development of the optimal NZSP controller developed above that there are no exogenous inputs to the system. A controller for autonomous air refueling must possess both stability robustness and performance robustness, since it must operate in the presence of both structured and unstructured uncertainties. The latter type of most interest to this problem is atmospheric turbulence. One technique to improve the disturbance accommodation properties of a controller to exogenous inputs is to pre-filter the control commands with a low pass filter. This will also reduce the risk of Pilot Induced Oscillations (PIO) by reducing control rates. An effective technique which permits the performance of the pre-filter to be tuned with quadratic weights is the Proportional-Integral-Filter (PIF) methodology, which is an extension of the optimal NZSP developed above. The resulting controller is termed Proportional Integral Filter - Nonzero Setpoint - Control Rate Weighting (PIF-NZSP-CRW), and a block diagram is shown in Fig.

14. Type-1 system performance is desired for the controller, so integrator states \mathbf{y}_{I_k} are defined such that the body-axis velocities u and v are integrated to x_{body} and y_{body} . To obtain the desired filtering of the controls, the controls are made states and augmented to the state vector. The optimal PIF-NZSP-CRW structure is derived by first defining the error of the integrated outputs as

$$\mathbf{y}_{I_{k+1}} = \mathbf{y}_k - \mathbf{y}_{m_k}; \quad \mathbf{y}_{I_{k+1}} \in \mathbb{R}^m \quad (46)$$

which upon substitution of Eq. (26) and Eq. (27) becomes

$$\begin{aligned} \mathbf{y}_{I_{k+1}} &= (H\mathbf{x}_k + D\mathbf{u}_k) - \mathbf{y}_{m_k} \\ &= H\mathbf{x}_k + D\mathbf{u}_k - H\mathbf{x}^* - D\mathbf{u}^* \\ &= H\hat{\mathbf{x}}_k + D\hat{\mathbf{u}}_k \end{aligned} \quad (47)$$

The augmented state-space system including the control rate states and integrated outputs is then

$$\tilde{\mathbf{x}}_{I_{k+1}} = \begin{bmatrix} \tilde{\mathbf{x}}_{k+1} \\ \tilde{\mathbf{u}}_{k+1} \\ \tilde{\mathbf{y}}_{k+1} + I \end{bmatrix} = \begin{bmatrix} \Phi & \Gamma & 0 \\ 0 & 0 & 0 \\ H & D & 0 \end{bmatrix} \begin{bmatrix} \tilde{\mathbf{x}}_k \\ \tilde{\mathbf{u}}_k \\ \tilde{\mathbf{y}}_k + I \end{bmatrix} + \begin{bmatrix} 0 \\ I \\ 0 \end{bmatrix} \tilde{\mathbf{u}}_{I_k} \quad (48)$$

and the quadratic cost function to be minimized is

$$\begin{aligned} J &= \frac{1}{2} \sum_{n=0}^{\infty} \left[\tilde{\mathbf{x}}_n^T \hat{Q} \tilde{\mathbf{x}}_n + \tilde{\mathbf{u}}_n^T \hat{R} \tilde{\mathbf{u}}_n + 2\tilde{\mathbf{x}}_n^T M \tilde{\mathbf{u}}_n + \tilde{\mathbf{u}}_{I_k}^T S_{\text{rate}} \tilde{\mathbf{u}}_{I_k} \right. \\ & \quad \left. + \mathbf{y}_{I_k}^T Q_2 \mathbf{y}_{I_k} \right] \end{aligned} \quad (49)$$

where the the matrix $S_{\text{rate}} \in \mathbb{R}^{m \times m}$ weights the control rates, and the matrix $Q_2 \in \mathbb{R}^{p \times p}$ weights the integrated outputs. Rearranging,

$$\begin{aligned} J &= \frac{1}{2} \sum_{n=0}^{\infty} \left[\tilde{\mathbf{x}}_{I_k}^T \begin{bmatrix} \hat{Q} & 0 & 0 \\ 0 & \hat{R} & 0 \\ 0 & 0 & Q_2 \end{bmatrix} \tilde{\mathbf{x}}_{I_k} + 2\tilde{\mathbf{x}}_n^T M \tilde{\mathbf{u}}_n \right. \\ & \quad \left. + \tilde{\mathbf{u}}_{I_k}^T S_{\text{rate}} \tilde{\mathbf{u}}_{I_k} \right] \end{aligned} \quad (50)$$

The minimizing control $\tilde{\mathbf{u}}_{I_k}$ is obtained from the solution to the matrix algebraic Riccati equation in infinite horizon

$$\begin{aligned} & \Phi^T P_{n+1} \Phi + \hat{Q} - (\Gamma^T P_{n+1} \Phi + M^T)^T \\ & \quad (\hat{R} + \Gamma^T P_{n+1} \Phi + M^T) = 0 \end{aligned} \quad (51)$$

which results in

$$\tilde{\mathbf{u}}_{I_k} = -K_1 \tilde{\mathbf{x}}_k - K_2 \tilde{\mathbf{u}}_k - K_3 \mathbf{y}_{I_k} \quad (52)$$

with K_1 the gain matrix for error states, K_2 the gain matrix for error controls, and K_3 the gain matrix for integrated outputs. Rewriting Eq. (52) in terms of the measured states and controls produces

$$\mathbf{u}_{I_k} = (\mathbf{u}_I^* + K_1 \mathbf{x}^* + K_2 \mathbf{u}^*) - K_1 \mathbf{x}_k - K_2 \mathbf{u}_k - K_3 \mathbf{y}_{I_k} \quad (53)$$

with all * quantities constant, except for the control rates, \mathbf{u}_I^* , which are equal to zero in steady-state. The constants \mathbf{x}^* and \mathbf{u}^* are solved for using (Eq. (37)). Upon substituting in Eq. (53) the control policy is

$$\mathbf{u}_{I_k} = (K_1 X_{12} + K_2 X_{22}) \mathbf{y}_m - K_1 \mathbf{x}_k - K_2 \mathbf{u}_k - K_3 \mathbf{y}_{I_k} \quad (54)$$

Note that in order to be admissible, this PIF-NZSP-CRW control policy requires measurement and feedback of all control positions, in addition to measurement and feedback of all states. As with the NZSP, the gains can be determined using any desired technique provided they are stabilizing. In this paper, the gains are designed using the Sampled Data Regulator (SDR) of Ref. 45.

The sampling frequency of the refueling boom docking controller is 10 Hz. Gains were designed by iterating on suitable choices of weights on the rates of θ_b , ψ_b , and d in the cost function

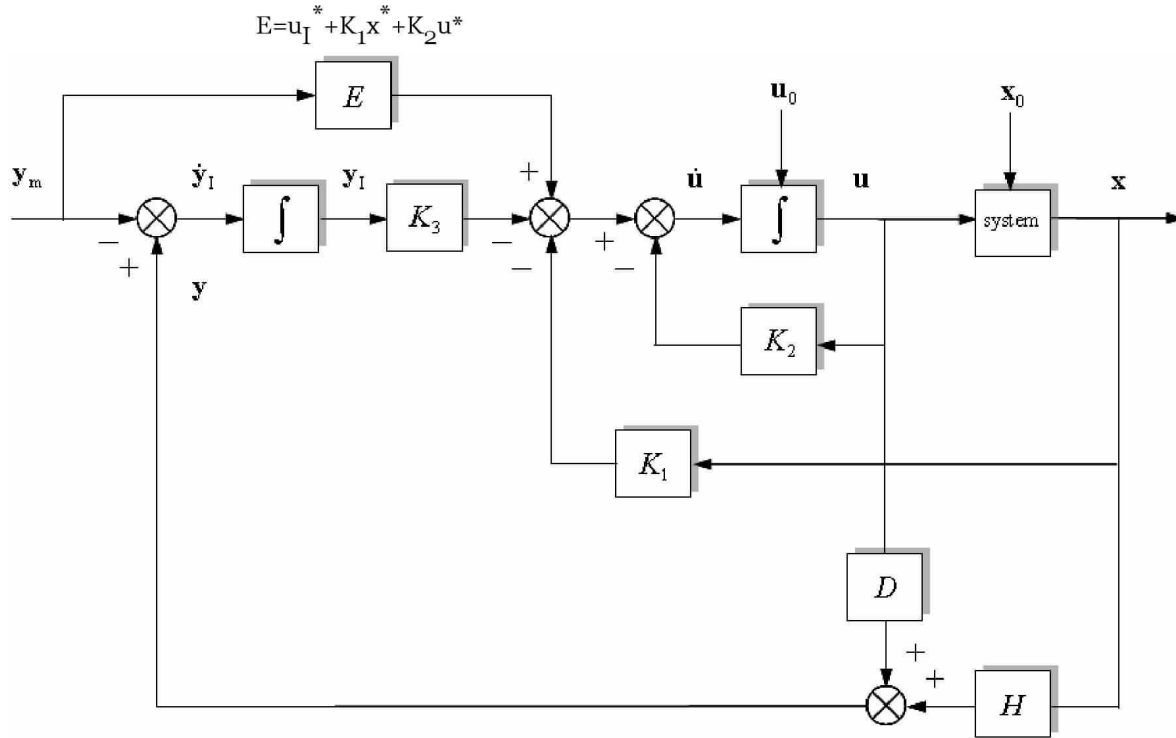


Figure 14: Proportional Integral Filter - Nonzero Setpoint - Control Rate Weighting Block Diagram

Eq. (50), until the control objective was satisfied within the specifications laid out in Section VIII.. Relative values between the weights indicate the contribution of particular states or controls in achieving the control objective. The highest preference is given to $\dot{\theta}_b$ in an effort to suppress oscillations of the boom, and several iterations resulted in a weight of 500. The next largest weight is a value of 15 given to the integral of θ_b for the purpose of eliminating hangoff errors in θ_b . Ruddervator control position and control rate were each given a weight of 10 to prevent position and rate limiting. Finally, extension of the boom was appropriately weighted to ensure that the controller does not extend the boom into the target receptacle until all vertical and lateral offset is eliminated. A weight of 0.0003 was found to successfully eliminate any steady-state error gradually and smoothly, as desired.

VII. Receiver and Tanker Station Keeping Controllers

The station keeping controller for maintaining the receiver UAV position within the refueling box is a full-state feedback sampled-data controller running at a sampling frequency of 10Hz. The gains are designed using the SDR technique, using the model in Section V. according to the synthesis procedure in Section VI.. Gains for the tanker aircraft station keeping controller were also designed using the model in Section V. and the SDR at a sampling frequency of 10Hz. For both discrete controllers, the SDR quadratic cost function to be minimized is

$$J = \frac{1}{2} \sum_{n=0}^{\infty} [\mathbf{x}_n^T \hat{Q} \mathbf{x}_n + \mathbf{u}_n^T \hat{R} \mathbf{u}_n + 2\mathbf{x}_n^T M \mathbf{u}_n] \quad (55)$$

The minimizing control is obtained from the solution to the matrix algebraic Riccati equation given in Eq. (31), resulting in the control law

$$\mathbf{u}_k = -K \mathbf{x}_k \quad (56)$$

with gain matrix

$$K_k = (\hat{R} + \Gamma^T P_{k+1} \Gamma)^{-1} (\Gamma^T P_{k+1} \Phi + M^T) \quad (57)$$

VIII. Simulation Examples

The examples demonstrate feasibility and performance of the visual snakes sensor system when integrated with the PIF-NZSP-CRW refueling boom docking controller for autonomous air refueling. The visual snake relative position estimates are obtained from a simulation of the system that includes calibrations, range effects, corrections due to optical distortions, and sensor noise. The navigation solution provides the receptacle position on the receiver UAV and attitude estimates directly to the controller. The visual snake optical sensor is mounted in the rear of the tanker aircraft above the refueling boom, looking down on the receiver UAV. The refueling receptacle on the receiver UAV is configured with a painted-on target consisting of a quadrilateral shape that appears as a square in the camera image plane when the receiver UAV is at the nominal refueling position. The control objective is to dock the tip of the refueling boom into the receptacle located on the nose of the receiver UAV, to an accuracy of ± 2 cm. An important requirement is to ensure that the refueling boom engages the receptacle with a relative velocity less than 0.5 m/sec, so as to minimize impact damage. The system is simulated for a flight condition of 250 knots true airspeed (KTAS) at 6,000m altitude, for test cases of still air and turbulent air. The nominal position of the receiver UAV is selected to be 4.5m behind and 3m below the trimmed position of the tanker aircraft.

A. Case I. Still Air

For the still air case, the receiver aircraft remains stationary in all axes, remaining at the nominal refueling position. The estimated values from the visual snakes sensor (Fig. 15) are seen to track the true values closely. As the refueling boom extends and then engages the receptacle, the displacements between the boom tip and the refueling receptacle on the UAV (Fig. 16) converge smoothly and quickly to zero while still satisfying the maximum docking speed requirement. All docking requirements are satisfied by approximately 28 seconds. Figure 17 shows that the boom controller smoothly steers the tip of the boom to the docking position,

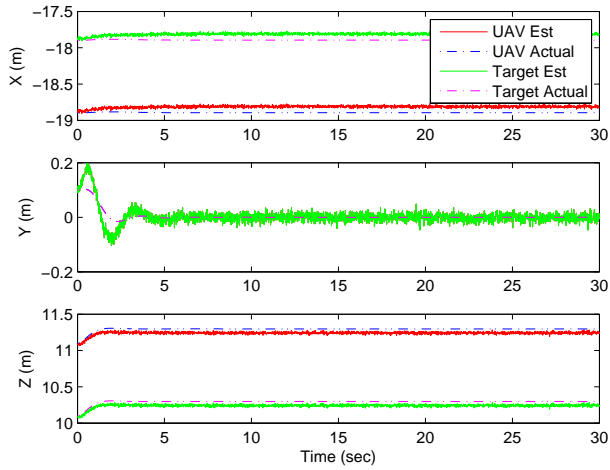


Figure 15: Case I Visual Snakes Navigation Sensor Position Estimation Errors, Still Air

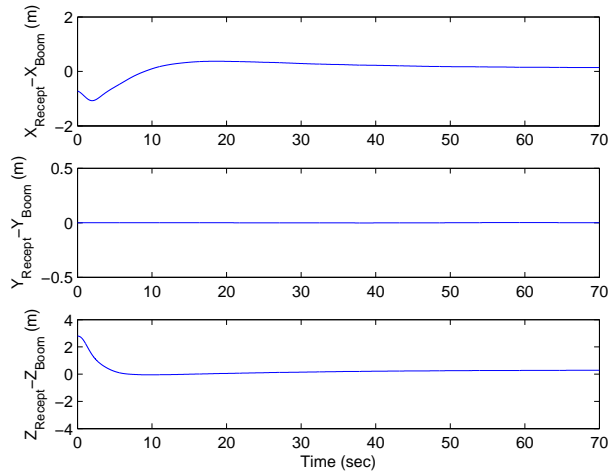


Figure 16: Case I Boom-Receptacle Relative Position Errors, Still Air

and Figures 18 and 19 show that the receiver UAV is well behaved during the maneuver, since all displacements and perturbations are small and well damped. As shown in Fig. 20, the control effector displacements are small, and all control rates (not shown) were well within limits.

B. Case II. Light turbulence

For this case both the tanker aircraft and the receiver UAV are subjected to light turbulence, and the receiver UAV is encountering the flowfield of the tanker. Figure 21 shows the estimated values from the visual snakes optical sensor. In spite of the motion of the receiver UAV relative to the sensor, good estimation is achieved. Figure 22 shows that the tip of the refueling boom tracks and mates with the movements of the receiver aircraft in the presence of light turbulence. Although the refueling boom trajectory slightly lags the receiver UAV trajectory, successful docking is achieved at approximately 32 seconds.

C. Case III. Moderate turbulence

For this case, both the tanker aircraft and the receiver UAV are subjected to moderate turbulence, and the receiver UAV is encountering the flowfield of the tanker. Figure 23 shows the estimated values from the visual snakes optical sensor. In spite of the motion of the receiver UAV relative to the sensor, good estimation is achieved. Figure 24 shows that the tip of the refueling boom tracks and mates with the movements of the receiver aircraft in the presence of moderate turbulence. As in the light turbulence case, the refueling boom trajectory lags the receiver aircraft trajectory, yet

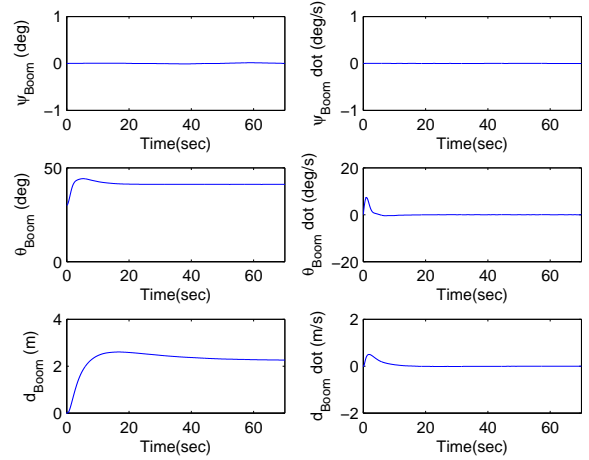


Figure 17: Case I Boom Displacement, Rotations, and Rates, Still Air

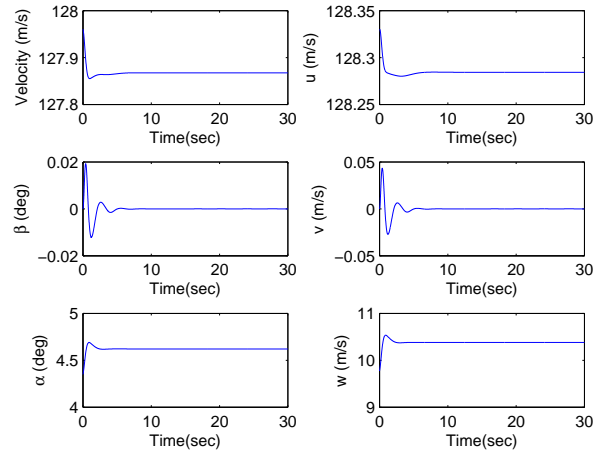


Figure 18: Case I Receiver Aircraft States, Still Air

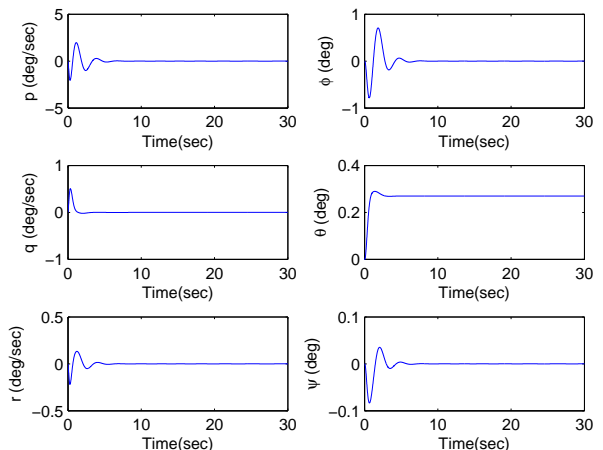


Figure 19: Case I Receiver Aircraft Angular States, Still Air

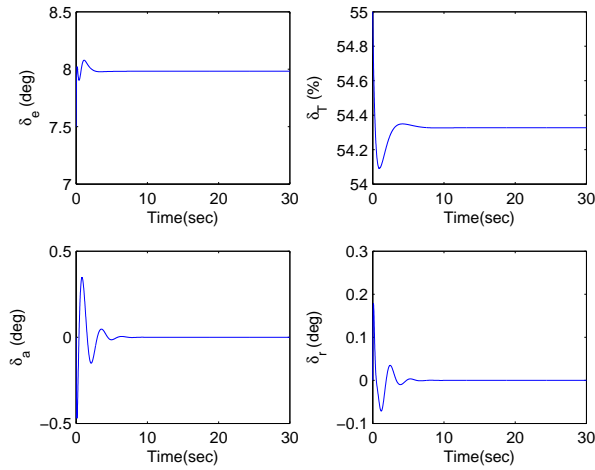


Figure 20: Case I Receiver Aircraft Control Effectors, Still Air

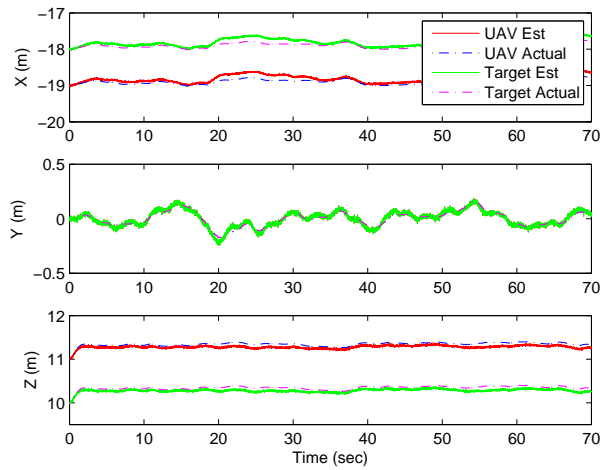


Figure 21: Case II Visual Snakes Navigation Sensor Position Estimation Errors, Light Turbulence

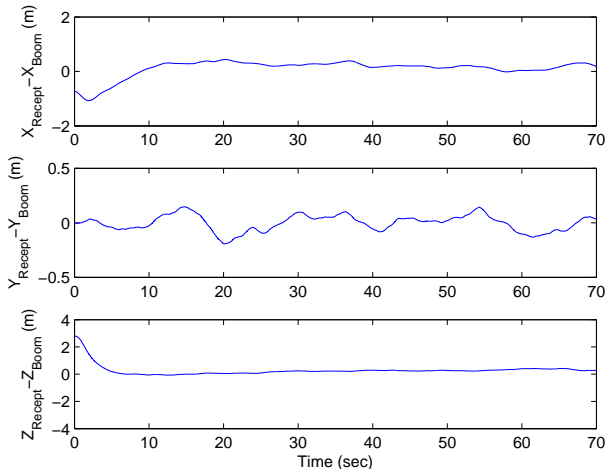


Figure 22: Case II Boom-Receptacle Relative Position Errors, Light Turbulence

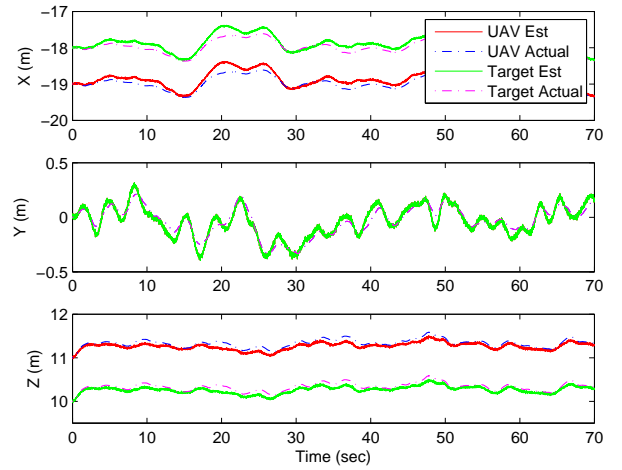


Figure 23: Case III Visual Snakes Navigation Sensor Position Estimation Errors, Moderate Turbulence

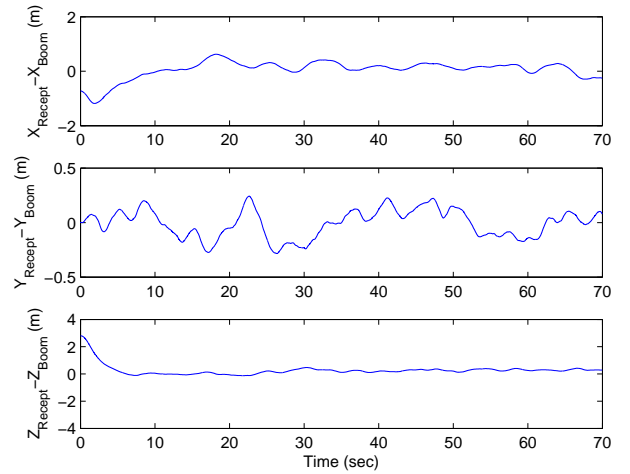


Figure 24: Case III Boom-Receptacle Relative Position Errors, Moderate Turbulence

achieves successful docking at approximately 37 seconds.

IX. Conclusions

This paper developed and demonstrated an accurate vision based sensor system for autonomous boom and receptacle air refueling. The visual snake optical sensor uses an active deformable contour algorithm that segments the target area of the image by having a closed, non-intersecting contour iterate across the image and track a target. The refueling boom docking controller is a sampled-data Proportional-Integral-Filter Nonzero Set Point Control-Rate-Weighting control law, which receives relative position measurements derived from the optical sensor and associated relative navigation algorithms. The integrated system is simulated for the case of autonomous air refueling of an Unmanned Air Vehicle from a tanker aircraft, in various levels of turbulence. Results demonstrate feasibility of the system for the autonomous air refueling task, within specifications of docking accuracy and maximum docking velocity. The disturbance accommodation properties of the refueling boom docking controller in turbulence are judged to be good, and provide a basis for optimism as regards to proceeding toward actual implementation.

X. Acknowledgments

The authors thank Felix Turcios, Monika Marwaha, and Amanda Lampton for contributions to the simulation models and controller.

Appendix

The tanker aircraft linear model is based upon data for the Boeing 747 from Ref. 43, for a steady, level, 1-g trimmed flight condition. The trim values are angle-of-attack $\alpha_1 = 2.5^\circ$, trim velocity $V_1 = 128.7$ m/sec, trim elevator deflection $\delta_{e_1} = 0^\circ$ and the trim engine power input $\delta_{T_1} = 50\%$. All translational quantities are in meters, and all angular quantities are in radians. Definitions for the variables in the state and control vectors are provided in Section V..

$$\mathbf{x}^T = [\delta X \quad \delta Y \quad \delta Z \quad u \quad \beta \quad \alpha \quad p \quad q \quad r \quad \phi \quad \theta \quad \psi]$$

$$A =$$

$$\begin{bmatrix} 0 & 0 & 0 & 0.99 & 0 & 5.67 & 0 & \dots & \dots & \dots & \dots & \dots \\ 0 & 0 & 0 & 0 & 128.7 & 0 & 0 & \dots & \dots & \dots & \dots & \dots \\ 0 & 0 & 0 & -0.044 & 0 & 128.57 & 0 & \dots & \dots & \dots & \dots & \dots \\ 0 & 0 & 0 & -0.0026 & 0 & -0.24 & 0 & \dots & \dots & \dots & \dots & \dots \\ 0 & 0 & 0 & 0 & -0.061 & 0 & -0.15 & \dots & \dots & \dots & \dots & \dots \\ 0 & 0 & 0 & -0.0005 & 0 & -0.38 & 0 & \dots & \dots & \dots & \dots & \dots \\ 0 & 0 & 0 & 0 & -0.39 & 0 & -0.45 & \dots & \dots & \dots & \dots & \dots \\ 0 & 0 & 0 & 0 & 0 & -0.026 & 0 & \dots & \dots & \dots & \dots & \dots \\ 0 & 0 & 0 & 0 & 0.043 & 0 & -0.028 & \dots & \dots & \dots & \dots & \dots \\ 0 & 0 & 0 & 0 & 0 & 0 & 1 & \dots & \dots & \dots & \dots & \dots \\ 0 & 0 & 0 & 0 & 0 & 0 & 0 & \dots & \dots & \dots & \dots & \dots \\ 0 & 0 & 0 & 0 & 0 & 0 & 0 & \dots & \dots & \dots & \dots & \dots \\ \dots & 0 & 0 & 0 & -18.42 & 0 & 0 & \dots & \dots & \dots & \dots & \dots \\ \dots & 0 & 0 & 0.014 & 0 & 422.6 & 0 & \dots & \dots & \dots & \dots & \dots \\ \dots & 0 & 0 & 0 & -421.8 & 0 & 0 & \dots & \dots & \dots & \dots & \dots \\ \dots & 17.98 & 0 & 0 & -32.19 & 0 & 0 & \dots & \dots & \dots & \dots & \dots \\ \dots & 0 & -3.25 & 0.25 & 0 & -0.011 & 0 & \dots & \dots & \dots & \dots & \dots \\ \dots & 3.2 & 0 & 0 & 0.0001 & 0 & 0 & \dots & \dots & \dots & \dots & \dots \\ \dots & 0 & 0.25 & 0 & 0 & 0 & 0 & \dots & \dots & \dots & \dots & \dots \\ \dots & -0.56 & 0 & 0 & 0.0004 & 0 & 0 & \dots & \dots & \dots & \dots & \dots \\ \dots & 0 & -0.103 & 0 & 0 & 0 & 0 & \dots & \dots & \dots & \dots & \dots \\ \dots & 0 & 0.044 & 0 & 0 & 0 & 0 & \dots & \dots & \dots & \dots & \dots \\ \dots & 1 & 0 & 0 & 0 & 0 & 0 & \dots & \dots & \dots & \dots & \dots \\ \dots & 0 & 1 & 0 & 0 & 0 & 0 & \dots & \dots & \dots & \dots & \dots \end{bmatrix}$$

$$\mathbf{u}^T = [\delta_e \quad \delta_T \quad \delta_a \quad \delta_r]$$

$$B = \begin{bmatrix} 0 & 0 & 0 & 0 \\ 0 & 0 & 0 & 0 \\ 0 & 0 & 0 & 0 \\ -0.16 & 19.57 & 0 & 0 \\ 0 & 0 & 0 & 0.039 \\ -0.071 & 5.99 & 0 & 0 \\ 0 & 0 & 0.069 & 0.095 \\ -0.41 & 0.34 & 0 & 0 \\ 0 & 0 & 0.0048 & -0.14 \\ 0 & 0 & 0 & 0 \\ 0 & 0 & 0 & 0 \\ 0 & 0 & 0 & 0 \end{bmatrix}$$

The receiver UAV linear model is obtained by linearizing a nonlinear simulation model from Ref. 5 about a steady, level, 1-g trimmed flight condition. The trim values are angle-of-attack $\alpha_1 = 4.35^\circ$, trim velocity $V_1 = 128.7$ m/sec, trim elevator deflection $\delta_{e_1} = 7.5^\circ$ and the trim engine power input $\delta_{T_1} = 55\%$. All translational quantities are in meters, and all angular quantities are in radians. Definitions for the variables in the state and control

vectors are provided in Section V..

$$\mathbf{x}^T = [\delta X \quad \delta Y \quad \delta Z \quad u \quad \beta \quad \alpha \quad p \quad q \quad r \quad \phi \quad \theta \quad \psi]$$

$$A =$$

$$\begin{bmatrix} 0 & 0 & 0 & 0.99 & 0 & 9.76 & 0 & \dots & \dots & \dots & \dots & \dots \\ 0 & 0 & 0 & 0 & 128.7 & 0 & 0 & \dots & \dots & \dots & \dots & \dots \\ 0 & 0 & 0 & -0.07 & 0 & 127.36 & 0 & \dots & \dots & \dots & \dots & \dots \\ 0 & 0 & 0 & -0.03 & 0 & 7.77 & 0 & \dots & \dots & \dots & \dots & \dots \\ 0 & 0 & 0 & 0 & -0.33 & 0 & 0.0008 & \dots & \dots & \dots & \dots & \dots \\ 0 & 0 & 0 & -0.0012 & 0 & -1.34 & 0 & \dots & \dots & \dots & \dots & \dots \\ 0 & 0 & 0 & 0 & -2.37 & 0 & -3.51 & \dots & \dots & \dots & \dots & \dots \\ 0 & 0 & 0 & -0.0015 & 0 & -2.57 & 0 & \dots & \dots & \dots & \dots & \dots \\ 0 & 0 & 0 & 0 & 2.76 & 0 & -0.033 & \dots & \dots & \dots & \dots & \dots \\ 0 & 0 & 0 & 0 & 0 & 0 & 1 & \dots & \dots & \dots & \dots & \dots \\ 0 & 0 & 0 & 0 & 0 & 0 & 0 & \dots & \dots & \dots & \dots & \dots \\ 0 & 0 & 0 & 0 & 0 & 0 & -0.0002 & \dots & \dots & \dots & \dots & \dots \\ \dots & 0 & 0 & 0 & 0 & -63.63 & 0 & \dots & \dots & \dots & \dots & \dots \\ \dots & 0 & 0 & 0.056 & 0 & 423.42 & 0 & \dots & \dots & \dots & \dots & \dots \\ \dots & 0 & 0 & 0 & -413.77 & 0 & 0 & \dots & \dots & \dots & \dots & \dots \\ \dots & -0.84 & 0 & 0 & -32.11 & 0 & 0 & \dots & \dots & \dots & \dots & \dots \\ \dots & 0 & -3.26 & 0.25 & 0 & -0.019 & 0 & \dots & \dots & \dots & \dots & \dots \\ \dots & 3.19 & 0 & 0 & 0 & 0 & 0 & \dots & \dots & \dots & \dots & \dots \\ \dots & 0 & 1.89 & 0 & 0 & 0 & 0 & \dots & \dots & \dots & \dots & \dots \\ \dots & -0.77 & 0 & 0 & 0 & 0 & 0 & \dots & \dots & \dots & \dots & \dots \\ \dots & 0 & -1.32 & 0 & 0 & 0 & 0 & \dots & \dots & \dots & \dots & \dots \\ \dots & 0 & 0.07 & 0 & 0 & 0 & 0 & \dots & \dots & \dots & \dots & \dots \\ \dots & 1 & 0 & 0 & 0 & 0 & 0 & \dots & \dots & \dots & \dots & \dots \\ \dots & 0 & 1 & 0 & 0 & 0 & 0 & \dots & \dots & \dots & \dots & \dots \end{bmatrix} \quad (58)$$

$$\mathbf{u}^T = [\delta_e \quad \delta_T \quad \delta_a \quad \delta_r]$$

$$B = \begin{bmatrix} 0 & 0 & 0 & 0 \\ 0 & 0 & 0 & 0 \\ 0 & 0 & 0 & 0 \\ 0.0081 & 0.26 & 0 & 0 \\ 0 & 0 & -0.0023 & 0.0035 \\ 0.0022 & 0.0018 & 0 & 0 \\ 0 & 0 & 0.52 & 0.07 \\ 0.12 & 0.014 & 0 & 0 \\ 0 & 0 & 0.024 & -0.09 \\ 0 & 0 & 0 & 0 \\ 0 & 0 & 0 & 0 \\ 0 & 0 & 0 & 0 \end{bmatrix}$$

The refueling boom linear model is obtained by linearizing a nonlinear boom dynamical model about the same flight conditions as the tanker aircraft. Definitions for the variables in the state and control vectors are provided in Section IV.. With values for the parameters $C_{d_b} = 0.045$, $C_{d_0} = 0.01$, $C_{d_\alpha} = 0.01$, $C_{l_\alpha} = 0.12$, $\phi = 0.73$ rad, $S = 1.2$ m², the model is:

$$\mathbf{x}^T = [\theta \quad \dot{\theta} \quad \psi \quad \dot{\psi} \quad d \quad \dot{d}]$$

$$A = \begin{bmatrix} 0 & 1 & 0 & 0 & 0 & 0 \\ -2.47 & 0 & 0 & 0 & -0.0094 & 0 \\ 0 & 0 & 0 & 1 & 0 & 0 \\ 0 & 0 & 0 & 0 & 0 & 0 \\ 0 & 0 & 0 & 0 & 0 & 1 \\ 0 & 0 & 0 & 0 & 0 & 0 \end{bmatrix}$$

$$\mathbf{u}^T = [\delta_{b_1} \quad \delta_{b_2} \quad \delta_d]$$

$$B = \begin{bmatrix} 0 & 0 & 0 \\ -0.32 & -0.32 & 0 \\ 0 & 0 & 0 \\ -0.48 & 0.48 & 0 \\ 0 & 0 & 0 \\ 0 & 0 & 1 \end{bmatrix}$$

References

- ¹Nalepka, J. P. and Hinchman, J. L., "Automated Aerial Refueling: Extending the Effectiveness of Unmanned Air Vehicles," *AIAA Modeling and Simulation Technologies Conference and Exhibit*, No. AIAA-2005-6005, San Francisco, California, 15-18 August 2005.
- ²Smith, R. K., "Seventy-Five Years of Inflight Refueling," *Air Force and Museums Program*, 1998.
- ³Pennington, R. J., "Tankers," *Air and Space Smithsonian*, Vol. 12, No. 4, November 1997, pp. 24-37.
- ⁴Maiersperger, W. P., "General Design Aspects of Flight Refueling," *Aeronautical Engineering Review*, Vol. 13, No. 3, March 1954, pp. 52-61.
- ⁵Valasek, J., Gunnam, K., Kimmet, J., Tandale, M. D., Junkins, J. L., and Hughes, D., "Vision-Based Sensor and Navigation System for Autonomous Air Refueling," *Journal of Guidance, Control, and Dynamics*, Vol. 28, No. 5, September-October 2005, pp. 832-844.
- ⁶Tandale, M. D., Bowers, R., and Valasek, J., "Robust Trajectory Tracking Controller for Vision Based Probe and Drogue Autonomous Aerial Refueling," *Journal of Guidance, Control, and Dynamics*, Vol. 29, No. 4, July-August 2006, pp. 846-857.
- ⁷Stepanyan, V., Lavretsky, E., and Hovakimyan, N., "Aerial Refueling Autopilot Design Methodology: Application to F-16 Aircraft Model," *AIAA Guidance, Navigation, and Control Conference and Exhibit*, Providence, Rhode Island, 16-19 August 2004, pp. AIAA-2004-5321.
- ⁸Barfield, A. F. and Hinchman, J. L., "An Equivalent Model for UAV Automated Aerial Refueling Research," *AIAA Modeling and Simulation Technologies Conference and Exhibit*, No. AIAA-2005-6006, San Francisco, California, 15-18 August 2005.
- ⁹Bloy, A. and Khan, M., "Modeling of the Receiver Aircraft in Air-To-Air Refueling," *Journal of Aircraft*, Vol. 38, No. 2, March-April 2001, pp. 393-396.
- ¹⁰Venkataramanan, S. and Dogan, A., "Dynamic Effects of Trailing Vortex with Turbulence & Time-Varying Inertia in Aerial Refueling," *AIAA Atmospheric Flight Mechanics Conference and Exhibit*, Providence, Rhode Island, 16-19 August 2004, pp. AIAA-2004-4945.
- ¹¹Fravolini, M., Ficola, A., Napolitano, M., Campa, G., and Perhinschi, M., "Development of Modeling and Control Tools for Aerial Refueling for UAVs," *AIAA Guidance, Navigation, and Control Conference and Exhibit*, No. AIAA-2003-5798, Austin, Texas, 11-14 August 2003.
- ¹²Blake, W. B., Dickes, E. G., and Gingras, D. R., "UAV Aerial Refueling - Wind Tunnel Results and Comparison with Analytical Predictions," *AIAA Atmospheric Flight Mechanics Conference and Exhibit*, Providence, Rhode Island, 16-19 August 2004, pp. AIAA-2004-4820.
- ¹³Williams, R. D., Feitshans, G. L., and Rowe, A. J., "A Prototype UAV Control Station Interface for Automated Aerial Refueling," *AIAA Modeling and Simulation Technologies Conference and Exhibit*, No. AIAA-2005-6009, San Francisco, California, 15-18 August 2005.
- ¹⁴Burns, R. S. and Clark, C. S., "The Automated Aerial Refueling Simulation at the AVTAS Laboratory," *AIAA Modeling and Simulation Technologies Conference and Exhibit*, No. AIAA-2005-6008, San Francisco, California, 15-18 August 2005.
- ¹⁵Dogan, A. and Sato, S., "Flight Control and Simulation for Aerial Refueling," *AIAA Guidance, Navigation, and Control Conference and Exhibit*, No. AIAA-2005-6264, San Francisco, California, 15-18 August 2005.
- ¹⁶Ochi, Y. and Kominami, T., "Flight Control for Automatic Aerial Refueling via PNG and LOS Angle Control," *AIAA Guidance, Navigation, and Control Conference and Exhibit*, No. AIAA-2005-6268, San Francisco, California, 15-18 August 2005.
- ¹⁷Stephenson, J. L., *The Air Refueling Receiver That Does Not Complain*, Ph.D. thesis, School of Advanced Airpower Studies Air University, Maxwell Air Force Base, Alabama, June 1998.
- ¹⁸Andersen, C. M., *Three Degree of Freedom Compliant Motion Control For Robotic Aircraft Refueling*, Master's thesis, Aeronautical Engineering, Air Force Institute of Technology, Wright-Patterson, Ohio, December 13 1990, AFIT/GAE/ENG/90D-01.
- ¹⁹Bennett, R. A., *Brightness Invariant Port Recognition For Robotic Aircraft Refueling*, Master's thesis, Electrical Engineering, Air Force Institute of Technology, Wright-Patterson, Ohio, December 13 1990, AFIT/GE/ENG/90D-04.
- ²⁰Shipman, R. P., *Visual Servoing For Autonomous Aircraft Refueling*, Master's thesis, Air Force Institute of Technology, Wright-Patterson, Ohio, December 1989, AFIT/GE/ENG/89D-48.
- ²¹Abidi, M. A. and Gonzalez, R. C., "The Use of Multisensor Data for Robotic Applications," *IEEE Transactions on Robotics and Automation*, Vol. 6, No. 2, April 1990, pp. 159-177.
- ²²Lachapelle, G., Sun, H., Cannon, M. E., and Lu, G., "Precise Aircraft-to-Aircraft Positioning Using a Multiple Receiver Configuration," *Proceedings of the National Technical Meeting, Institute of Navigation*, Inst of Navigation, Alexandria, VA, 1994, pp. 793-799.
- ²³Campa, G., Seanor, B., Perhinschi, M., Fravolini, M., Ficola, A., and Napolitano, M., "Autonomous Aerial Refueling for UAVs Using a Combined GPS-Machine Vision Guidance," *AIAA Guidance, Navigation, and Control Conference and Exhibit*, Providence, Rhode Island, 16-19 August 2004, pp. AIAA-2004-5350.
- ²⁴Vendra, S., *Addressing Corner Detection Issues for Machine Vision based UAV*, Master's thesis, College of Engineering and Mineral Resources, West Virginia University, Morgantown, West Virginia, March 2006, Aerospace Engineering Department.
- ²⁵Junkins, J. L., Hughes, D., Wazni, K., and Pariyapong, V., "Vision-Based Navigation for Rendezvous, Docking, and Proximity Operations," *22nd Annual ASS Guidance and Control Conference*, No. ASS-99-021, Breckenridge, Colorado, February 1999.
- ²⁶Alonso, R., Crassidis, J. L., and Junkins, J. L., "Vision-Based Relative Navigation for Formation Flying of Spacecraft," No. AIAA-2000-4439, American Institute of Aeronautics and Astronautics, 2000.
- ²⁷Gunnam, K., Hughes, D., Junkins, J. L., and Nasser, K.-N., "A DSP Embedded Optical Navigation System," *Proceedings of the Sixth International Conference on Signal Processing (IC SP '02)*, Beijing, People's Republic of China, August 2002.
- ²⁸Kimmet, J., Valasek, J., and Junkins, J. L., "Autonomous Aerial Refueling Utilizing A Vision Based Navigation System," *Proceedings of the AIAA Guidance, Navigation, and Control Conference*, No. AIAA-2002-4469, Monterey, CA, 5-8 August 2002.
- ²⁹Kimmet, J., Valasek, J., and Junkins, J. L., "Vision Based Controller for Autonomous Aerial Refueling," *Proceedings of the IEEE Control Systems Society Conference on Control Applications*, No. CCA02-CCAREG-1126, Glasgow, Scotland, Sep. 2002.
- ³⁰Valasek, J. and Junkins, J. L., "Intelligent Control Systems and Vision Based Navigation to Enable Autonomous Aerial Refueling of UAVs," *27th Annual AAS Guidance and Control Conference*, No. AAS 04-012, Breckenridge, CO, Feb. 2004.
- ³¹Kass, M., Witkin, A., and Terzopoulos, D., "Snakes: active contour models," *International Journal of Computer Vision*, Vol. 1, No. 4, 1987, pp. 321-331.
- ³²Schaub, H. and Smith, C. E., "Color Snakes for Dynamic Lighting Conditions on Mobile Manipulation Platforms," *IEEE/RIS International Conference on Intelligent Robots and Systems*, Las Vegas, NV, Oct. 2003.
- ³³Perrin, D. and Smith, C. E., "Rethinking Classical Internal Forces for Active Contour Models," *Proceedings of the IEEE International Conference on Computer Vision and Pattern Recognition*, Vol. 2, Dec. 8-14 2001, pp. 615-620.
- ³⁴Smith, C. E. and Schaub, H., "Efficient Polygonal Intersection Determination with Applications to Robotics and Vision," *IEEE/RSJ International Conference on Intelligent Robots and Systems*, Edmonton, Alberta, Canada, Aug. 2-6 2005.
- ³⁵Monda, M. and Schaub, H., "Spacecraft Relative Motion Estimation using Visual Sensing Techniques," *AIAA Infotech@Aerospace Conference*, Arlington, VA, Sept. 26-29 2005, Paper No. 05-7116.
- ³⁶Kass, M., Witkin, A., and Terzopoulos, D., "Snakes: Active contour models," *International Journal of Computer Vision*, Vol. 1, No. 4, 1987, pp. 321-331.
- ³⁷Perrin, D. P., Ladd, A. M., Kavradi, L. E., Howe, R. D., and Cannon, J. W., "Fast Intersection Checking for Parametric Deformable Models," *SPIE Medical Imaging*, San Diego, CA, February 12-17 2005.
- ³⁸Malladi, R., Kimmel, R., Adalsteinsson, D., Sapiro, G., Caselles, V., and Sethian, J. A., "A geometric approach to segmentation and analysis of 3D medical images," *Proceedings of Mathematical Methods in Biomedical Image Analysis Workshop*, San Francisco, June 21-22 1996.
- ³⁹Ivins, J. and Porrill, J., "Active Region Models for Segmenting Medical Images," *Proceedings of the IEEE International Conference on Image Processing*, Austin, Texas, 1994, pp. 227-231.
- ⁴⁰Schaub, H. and Wilson, C., "Matching a Statistical Pressure Snake to a Four-Sided Polygon and Estimating the Polygon Corners," Technical Report SAND2004-1871, Sandia National Laboratories, 2003.
- ⁴¹Smith, A. and Kunz, D., "Dynamic Coupling of the KC-135 Tanker and Boom for Modeling and Simulation," *AIAA Modeling and Simulation Technologies Conference and Exhibit*, No. AIAA-2006-6480, Keystone, Colorado, 21-24 August 2006.
- ⁴²Hoak, D. E., "USAF Stability and Control DATCOM," Tech. Report Contract AF33(616)-6460, Air Force Flight Dynamics Laboratory, Wright-Patterson Air Force Base, OH, October 1960.
- ⁴³Roskam, J., *Airplane Flight Dynamics and Automatic Flight Controls, Part I*, Vol. 1, Design, Analysis, and Research Corporation, Lawrence, KS, 1994, p. 236.
- ⁴⁴Junkins, J. L. and Kim, Y., *Introduction to Dynamics and Control of Flexible Structures*, American Institute of Aeronautics and Astronautics, Washington, DC, 1993, pp. 10-14.
- ⁴⁵Dorato, P., "Optimal Linear Regulators: The Discrete-Time Case," *IEEE Transactions on Automatic Control*, Vol. AC-16, No. 6, December 1971, pp. 613-620.